

Topology Optimization of Two Fluid Heat Exchangers

Lukas Christian Høghøj^{a,*}, Daniel Ruberg Nørhave^a, Joe Alexandersen^b, Ole Sigmund^a, Casper Schousboe Andreassen^a

^aDepartment of Mechanical Engineering, Section for Solid Mechanics, Technical University of Denmark, Kgs. Lyngby, Denmark

^bDepartment of Mechanics and Electronics, Section of Mechanical Engineering, University of Southern Denmark, Odense, Denmark

Abstract

A method for density-based topology optimization of heat exchangers with two fluids is proposed. The goal of the optimization process is to maximize the heat transfer from one fluid to the other, under maximum pressure drop constraints for each of the fluids. A single design variable is used to describe the physical fields. The solid interface and the fluid domains are generated using an erosion-dilation based identification technique, which guarantees well-separated fluids, as well as a minimum wall thickness between them. Under the assumption of laminar steady flow, the two fluids are modelled separately, but in the entire computational domain using the Brinkman penalization technique for ensuring negligible velocities outside of the respective fluid subdomains. The heat transfer is modelled using the convection-diffusion equation, where the convection is driven by both fluid flows. A stabilized finite element discretization is used to solve the governing equations. Results are presented for two different problems: a two-dimensional case illustrating and verifying the methodology; and a three-dimensional case inspired by shell-and-tube heat exchangers. The optimized designs for both cases show an improved heat transfer compared to the baseline designs. For the shell-and-tube case, the full freedom topology optimization approach is shown to yield performance improvements of up to 113% under the same pressure drop.

Keywords: Topology Optimization, Heat Exchanger, Interface identification, Forced Convection, Multiphysics optimization

Nomenclature

Physics

α Impermeability

C_k Thermal conductivity ratio

ΔP Pressure drop

\dot{m} Mass flow

ϵ Effectiveness

Da Darcy number

NTU Number of Transfer Units

Nu Nusselt number

UA Overall heat transfer coefficient

μ Dynamic viscosity

Pe Peclet number

Pe_s Solid Peclet number

Re Reynolds number

ρ Density

c_p Heat capacity

k Conductivity

L Length

n Normal

P Dynamic pressure

T Temperature

u Velocity

w_e Wall thickness

x Coordinate

*Please address correspondence to luch@mek.dtu.dk

Optimization

β	Heaviside projection sharpness
λ	Lagrangian multiplier
η	Heaviside projection threshold
\mathcal{L}	Lagrangian function
Φ	Objective function
ξ	Design variable
ξ_γ	Mapped design variables
$\hat{\xi}$	Filtered design variable
$\hat{\hat{\xi}}$	Re-filtered design variable
$\hat{\xi}_\gamma$	Eroded and dilated re-filtered design variable
$\tilde{\xi}$	Projected design variable
g	Constraint function
p_k	Penalization power
q	RAMP curvature parameter
r	Filter radius

Subscripts

<i>base</i>	Baseline design
<i>Fγ</i>	Fluid γ
<i>initial</i>	Initial (start of optimization) design
<i>in</i>	Inlet
<i>out</i>	Outlet
<i>T</i>	Heat transfer
<i>w</i>	Wall

Superscripts

γ	Fluid index
----------	-------------

1. Introduction

Heat exchangers are devices that serve to transfer thermal energy between two or more fluids, usually separated by solid walls to avoid mixing. They can be used for both cooling and heating applications, with some of the most well-known applications being combustion engine cooling, air conditioning, power production and refrigeration.

Heat exchangers are widely used and their analysis is covered in most basic heat transfer courses and any good book on heat transfer, e.g. [1]. They are typically dimensioned and designed based on classical heat transfer theory under certain assumptions for predefined geometric layouts [2]. In recent time, the use of computational fluid dynamics (CFD) and conjugate heat transfer (CHT) simulations has become an indispensable tool for the analysis and design of complex heat exchangers [3]. However, their designs are still mainly restricted to classical, and rather simple, geometries, such as parallel flow, counter-flow and cross-flow heat exchangers, as illustrated in Figure 1. These can be assembled from standard components and manufacturing processes, e.g. punching and brazing, ensuring easy mass production at low cost.

Recent advances within additive manufacturing of conductive metals have spurred an increase in the internal geometric complexity of new heat exchanger designs [4, 5]. However, emphasis is put on maximizing the internal interacting surface area, using for instance Triply Periodic Minimal Surfaces (TPMS) [5]. This relies on a critical assumption based on Newton's law of cooling for the heat flux due to convection $q_{\text{conv}} = h A_s (T_s - T_\infty)$, where h is the convection heat transfer coefficient, A_s is the area of the heat transfer surface, T_s is the temperature of the surface and T_∞ is the fluid reference temperature. It seems obvious to increase the surface area, A_s , to increase the heat flux. However, an increase in the surface area due to increasing geometric complexity almost certainly leads to a decrease in the convection coefficient, h , since the fluids will flow slower due to a higher flow resistance. Of course, one can always use a more powerful pump to circumvent this, but the increased energy input must be weighted by the overall efficiency of the heat exchanger. Therefore, this paper proposes a novel approach for the simulation-driven design optimization of pressure-drop-constrained two-fluid heat exchangers with a separating solid conductive wall using topology optimization. The approach optimizes the heat exchanger by a direct measure of the heat exchanger efficiency, based on simulations, rather than an implicit geometric quantity such as

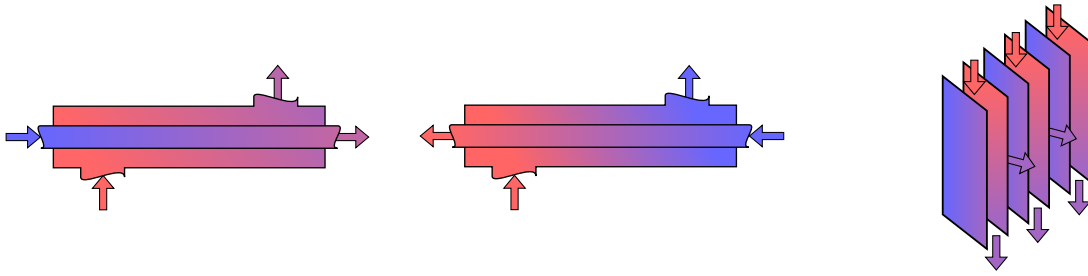


Figure 1: Illustration of common heat exchanger configurations. From left: Parallel flow, counter-flow and cross-flow heat exchangers.

the surface area. An erosion-dilation based identification technique inspired by Luo et al. [6] is used to obtain the solid wall. This procedure allows for a control of the minimum wall thickness. Furthermore, the 3D implementation allows for large design freedom, where channels and other features can cross, which is not possible in planar implementations.

Topology optimization is a computational design methodology for optimizing structures. It originated in the field of solid mechanics [7] and has seen widespread use there [8] over the past three decades. As detailed in the recent review paper by Alexandersen and Andreassen [9], topology optimization has been applied to a wide range of flow-based problems since the first application to Stokes flow by Borrvall and Petersson [10] in 2003. In order to apply topology optimization to heat exchanger design, it is necessary to be able to treat three-dimensional problems with high mesh resolutions. The three-dimensionality is necessary to model the complex interactions of most heat exchangers and the high mesh resolution is mainly necessary to provide a high design freedom for topology optimization by resolving small features (e.g. thin solid walls). For large scale three-dimensional flow-based problems, previous works have treated pure fluid flow [11, 12, 13, 14, 15, 16, 17] and conjugate heat transfer problems for forced convection [18, 19, 20, 21, 22, 23] and natural convection [24, 25, 26].

In the context of topology optimization, literature on the design of heat exchangers is very sparse. Two papers have treated guiding channels or winglets for fin-and-tube heat exchangers [27, 28]. However, they only consider additional flow guiding features for existing heat exchanger geometries. Only a few works consider the design of the actual heat exchanger solid surface geometry using topology optimization. The first is the M.Sc. thesis by Papazoglou [29] investigating both a fluid tracking model and a multi-fluid model for a density-based approach. The second is the Ph.D. thesis by Haertel [30] coupling two-dimensional in-plane and

out-of-plane flow models using an interface model similar to our approach. The third is the paper by Tawk et al. [31] proposing a density-based multi-fluid approach for optimizing heat exchangers with two separate fluids and a solid. The fourth is the conference paper by Saviers et al. [32] which, however, provides very little technical details on the applied methodology. Finally, very recently, after the completion of the present work, a preprint was uploaded to *arXiv.org* by Kobayashi et al. [33]. The authors also use a single design variable to parametrize two fluids and a solid. The solid is represented by intermediate design variable values, whose existence is guaranteed due to filtering of the design field. However, the approach does not appear to have thickness control of the solid and is only applied to smaller computational problems.

Interface identification techniques are used to capture the transition from one physical phase to another. Such a technique was introduced by Clausen et al. [34, 35] for topology optimization of coated structures. The method uses the spatial gradient of the design variable to identify where coating should be applied. More recently, a modified formulation was introduced by Luo et al. [6], where the design field is eroded and dilated, with the intersection of these fields identifying the interface.

The paper is organized as follows: Section 2 introduces the parametrization and states the goal and constraint of the optimization problem; Section 3 details the physics of the problem and the assumptions made; Section 4 provides an brief description of the finite element formulation; Section 5 presents the proposed topology optimization methodology; Section 6 show optimized heat exchangers for two numerical examples; and Section 7 provides a discussion and conclusions.

2. Parametrization

The goal of the optimization problem is to maximize the heat transferred in a heat exchanger at a given opera-

129 tional power, which is proportional to the pressure drop
130 across the heat exchanger.

131 The problem concerns the arrangement of a solid inter-
132 face, which separates the two fluids, as illustrated in
133 Figure 2. The fluid domains are denoted Ω^γ , where
134 superscript γ is the fluid index, and are separated by a solid
135 domain Ω^s . The total computational domain is given
136 as the union of all subdomains, $\Omega = \Omega^1 \cup \Omega^2 \cup \Omega^s$.
137 In order to introduce the design representation the non-
138 overlapping domain representation is relaxed, such that
139 both fluids may be present in the entire domain. How-
140 ever, by the use of an identification technique, every
141 point in the domain is sought to be exclusively assigned
142 either as one of the two fluids or as solid. This means
143 that the velocity of a fluid should be zero outside of its
144 domain Ω^γ .

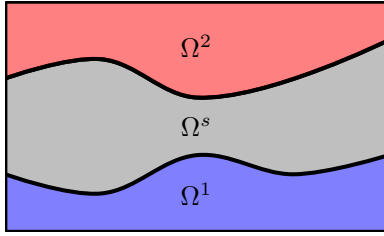


Figure 2: Sketch of the subdomains in the domain of interest. The Ω^1 (blue) and Ω^2 (red) domains are the domains of fluids 1 and 2, respectively. The solid domain, Ω^s (grey), separates the two fluids.

145 3. Governing equations

146 A two fluid heat exchanger contains two mass trans-
147 fer problems (one for each fluid) and one global heat
148 transfer problem. The governing equations are de-
149 rived under the assumption of steady state, constant
150 fluid properties and incompressibility. Furthermore,
151 heat generated by viscous dissipation is neglected. The
152 stated assumptions result in a weak coupling between
153 the mass and heat transfer, as only the mass transfer af-
154 fects the heat transfer, but not the other way around.

155 In the following, the governing equations are pre-
156 sented in their dimensionless form.

157 3.1. Mass transfer

158 The mass transfer for each of the fluid domains is
159 obtained by solving the dimensionless Navier-Stokes
160 equations. The equations for each mass transfer are
161 posed in the entire domain Ω to permit topology opti-
162 mization. A Brinkman friction term is used to penalize
163 fluid flow outside the fluid subdomain [10, 36, 37].

164 For each fluid, denoted by index¹ γ the non-
165 dimensional equations yield:

$$166 u_i^\gamma \frac{\partial u_j^\gamma}{\partial x_i} - \frac{1}{Re^\gamma} \frac{\partial}{\partial x_i} \left(\frac{\partial u_i^\gamma}{\partial x_j} + \frac{\partial u_j^\gamma}{\partial x_i} \right) + \frac{\partial P^\gamma}{\partial x_i} = -\alpha^\gamma(\mathbf{x}) u_i^\gamma \quad (1)$$

$$167 \frac{\partial u_i^\gamma}{\partial x_i} = 0 \quad (2)$$

168 where u is velocity, P the dynamic pressure and α the
169 impermeability. The Reynolds number, Re , is a dimen-
170 sionless parameter indicating the ratio between the iner-
171 tial and the viscous forces in the flow. It is expressed as
a function of a reference velocity, U , a length scale L ,
the fluid mass density ρ and dynamic viscosity μ :

$$172 Re = \frac{UL\rho}{\mu} \quad (3)$$

173 The impermeability, $\alpha(\mathbf{x})$, is defined for each point in
the domain:

$$174 \alpha^\gamma(\mathbf{x}) = \begin{cases} 0 & \text{if } \mathbf{x} \in \Omega^\gamma \\ \infty & \text{if } \mathbf{x} \notin \Omega^\gamma \end{cases} \quad (4)$$

175 where it is seen that the impermeability is always $\alpha^\gamma =$
176 ∞ outside of fluid γ . In practice, the impermeability can
177 not be set to $\alpha = \infty$ for numerical reasons. Instead, a
178 large value is used. For consistency, the impermeability
179 outside of the fluid region is related to the Darcy number
[38] and is given as:

$$\bar{\alpha}^\gamma = \frac{1}{Re^\gamma} \frac{1}{Da} \quad (5)$$

180 The mass transfer problems are subject to homoge-
181 neous Dirichlet boundary conditions on the velocity at
182 the domain boundaries, not being in- or outlets. A ho-
183 mogeneous Dirichlet boundary condition is placed on
184 the pressure at the outlet.

185 3.2. Heat transfer

186 The heat transfer is described by the convection-
187 diffusion equation. The equation is non-
188 dimensionalised using the solid conductivity, k^s .
189 As the velocities are assumed to be $u_i^\gamma = 0$ outside
190 of their respective corresponding domain Ω^γ , the heat
191 transfer in the entire computational domain Ω can be
192 expressed as:

$$\sum_{\gamma=1}^{NF} (Pe_s^\gamma u_i^\gamma) \frac{\partial T}{\partial x_i} - \frac{\partial}{\partial x_i} \left(C_k(\mathbf{x}) \frac{\partial T}{\partial x_i} \right) = 0 \quad (6)$$

¹Unlike for subscripts, a repeated superscript γ does not imply summation over the index.

193 where Pe_s^γ is the solid Peclet number, which relates 232
 194 the convective heat transfer in a fluid to the diffusive 233
 195 heat transfer in the solid. The conductivity ratio, C_k ,
 196 is the conductivity normalized by the solid conductiv-
 197 ity. These parameters can be linked to the conventional
 198 Peclet number of each fluid:

$$Pe_s^\gamma = \frac{\rho^\gamma c_p^\gamma UL}{k^s}, \quad C_k^\gamma = \frac{k^\gamma}{k^s}, \quad Pe^\gamma = \frac{Pe_s^\gamma}{C_k^\gamma} \quad (7)$$

199 The heat transfer problem is modelled by one equation
 200 for the entire domain Ω , with a spatially varying coeffi-
 201 cient C_k defined by:

$$C_k(\mathbf{x}) = \begin{cases} C_k^\gamma & \text{if } \mathbf{x} \in \Omega^\gamma \\ 1 & \text{if } \mathbf{x} \in \Omega^s \end{cases} \quad (8)$$

202 The boundary conditions for the heat transfer problem
 203 consist of Dirichlet boundary conditions at the respec-
 204 tive fluid inlets. On the rest of the domain boundary,
 205 a homogeneous Neumann boundary condition is im-
 206 posed, resulting in the design domain being externally
 207 insulated.

208 4. Finite element formulation

209 The equation system is discretized and solved us-
 210 ing the Finite Element Method (FEM), using struc-
 211 tured meshes with regular trilinear hexahedral elements.
 212 PSPG stabilization is employed to facilitate the use of
 213 equal-order elements. SUPG stabilization is applied to
 214 both mass transfer problems and the heat transfer prob-
 215 lem to alleviate problems with steep gradients due to
 216 convection. The implementation from [24] is reused
 217 here without the Boussinesq approximation terms. As
 218 the coupling between the mass and heat transfer consid-
 219 ered here is weak, the problems are solved sequentially.

220 The two mass transfer problems are solved by finding
 221 the solution to the vector of residual equations given by:

$$\mathbf{R}_{F\gamma} = \mathbf{M}(\mathbf{u}_{F\gamma}, \alpha_\gamma) \mathbf{u}_{F\gamma} - \mathbf{b}_{F\gamma} = \mathbf{0} \quad (9)$$

222 The solution vector $\mathbf{u}_{F\gamma}$ contains all three velocity com-
 223 ponents and the pressure for every node. The system
 224 matrix $\mathbf{M}(\mathbf{u}_{F\gamma}, \alpha_\gamma)$ contains the viscosity, convection,
 225 Brinkman penalization, pressure coupling and velocity
 226 divergence contributions, as well as all the correspond-
 227 ing SUPG and PSPG stabilization terms. The weak
 228 form and stabilization parameters are detailed in Ap-
 229 pendix A.1.

230 Similarly, the residual equations for the heat transfer
 231 problem are defined as:

$$\mathbf{R}_T = \mathbf{M}_T(\mathbf{C}_k, \mathbf{u}_{Pe}) \mathbf{T} - \mathbf{b}_T = \mathbf{0} \quad (10)$$

where the system is built based on the global velocity
 field combining both fluid flows:

$$\mathbf{u}_{Pe} = Pe_s^1 \mathbf{u}_{F1} + Pe_s^2 \mathbf{u}_{F2} \quad (11)$$

234 which is possible due to the assumption of the fluid do-
 235 mains being well-separated at the final design. The so-
 236 lution vector \mathbf{T} contains the temperature in every node
 237 and the system matrix $\mathbf{M}_T(\mathbf{C}_k, \mathbf{u}_{Pe})$, is assembled from
 238 the thermal diffusion, convection and SUPG stabiliza-
 239 tion contributions. The weak form of these contribu-
 240 tions, as well as the stabilization parameter, are detailed
 241 in Appendix A.2.

242 5. Topology optimization

243 5.1. Optimization problem

244 The generic optimization problem is given as the
 245 minimization of the objective function Φ , subject to
 246 m constraints g_i . Furthermore, a nested formulation is
 247 used where the residuals of the mass- and heat transfer
 248 problems from (9) and (10), are assumed zero in each
 249 iteration. The design variable ξ is relaxed from discrete
 250 $\xi \in \{0, 1\}$ to continuous $\xi \in [0, 1]$ and represented by n
 251 elementwise constant scalars.

$$\begin{aligned} \min_{\xi \in [0, 1]^n} \quad & \Phi(\xi, u^1, u^2, T) \\ \text{s.t.} \quad & \mathbf{R}_{F\gamma} = 0, \quad \gamma = \{1; 2\} \\ & \mathbf{R}_T = 0 \\ & g_i \leq 0, \quad i = 1 \dots m \end{aligned} \quad (12)$$

252 The objective function for a heat exchanger is to max-
 253 imize the thermal energy transferred from the hot to the
 254 cold fluid. This can be expressed as minimizing the dif-
 255 ference between the enthalpy flowing out at the cooled
 256 and coolant fluid outlets²:

$$\Phi = \frac{1}{\int_{\Gamma_{F2}} dA} \left(Pe_s^1 \int_{\Gamma_{F1}} n_i u_i^1 T dA - Pe_s^2 \int_{\Gamma_{F2}} n_i u_i^2 T dA \right) \quad (13)$$

257 This objective function has the advantage of being de-
 258 fined on both fluid outlets, which it is beneficial for the
 259 computation of the sensitivities, as both mass transfer
 260 adjoint problems will have a source term on their re-
 261 spective outlets. However, it can be difficult to associate
 262 physical meaning to it. Therefore, for comparison pur-
 263 poses, we introduce $\Phi_{coolant}$, which is an expression of

²Figure 5 shows the formal definition of the inlet and outlet re-
 gions.

264 the heat transferred to the coolant, normalized by the
265 outlet area:

$$\Phi_{coolant} = \frac{Pe_s^2}{\int_{\Gamma_{F2}} dA} \int_{\Gamma_{F2}} n_i u_i^2 T dA \quad (14)$$

266 where a higher value is preferred since it reflect the
267 amount of heat transferred to the coolant from the other
268 fluid.

269 In order to regularize the geometry, and impose re-
270 strictions on the pumping power, the pressure drop on
271 each fluid phase is controlled. This is done by placing a
272 pressure drop constraint on each of the fluids:

$$g_\gamma = \frac{1}{\Delta P_{max}^\gamma \int_{\Gamma_{in, F\gamma}} dA} \int_{\Gamma_{in, F\gamma}} P^\gamma dA - 1 \quad (15)$$

273 where ΔP_{max}^γ is the maximal admissible pressure drop
274 on fluid γ .

275 The optimization problem is solved using the Method
276 of Moving Asymptotes (MMA) [39], implemented in
277 PETSc [40] using external move limits of 0.2.

278 5.2. Filtering and projecting

279 In topology optimization, filtering techniques are
280 used to prevent checkerboards and other unwanted ef-
281 fects from appearing in the obtained designs [41]. The
282 PDE filter [42, 40] is here used to obtain a filtered de-
283 sign field $\hat{\xi}$:

$$-R^2 \nabla^2 \hat{\xi} + \hat{\xi} = \xi \quad (16)$$

$$R = \frac{r}{2\sqrt{3}} \quad (17)$$

284 where r is the physical filter radius.

285 A smooth Heaviside projection [43] with threshold η
286 and sharpness β is applied to the filtered variable, which
287 leads to the projected field $\tilde{\xi}$:

$$\tilde{\xi}(\hat{\xi}, \beta, \eta) = \frac{\tanh(\beta\eta) + \tanh(\beta(\hat{\xi} - \eta))}{\tanh(\beta\eta) + \tanh(\beta(1 - \eta))} \quad (18)$$

288 In combination with the filter, the Heaviside projec-
289 tion, can be used to enforce a minimum length scale on
290 the obtained structures [43] if multiple design realiza-
291 tions are considered.

292 5.3. Modelling solid interfaces

293 A single design variable, ξ , is used to model three
294 physical phases: two fluids and one solid. In order to en-
295 sure strict separation between the two fluid phases, it is
296 important that there always exists a solid wall between
297 them. A method for the introduction of a third phase

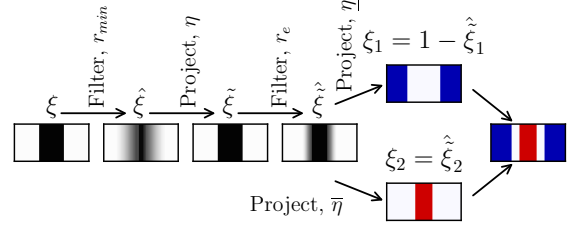


Figure 3: Overview of the different variables used in the erosion-dilatation process. The resulting variables ξ_1 and ξ_2 are used to define the domains of the two fluids (red and blue) and of the solid interfaces (white).

298 between two already existing ones, has been introduced
299 for minimization of elastic compliance of coated struc-
300 tures [34, 35, 6]. In its original application, the purpose
301 of this method is to introduce a coating of a specific
302 thickness between the void and the solid. In the present
303 case, solid is placed between two fluids and allows for
304 rigorous control of the interface thickness.

305 As seen in Figure 3, the process consists of a filtering
306 operation with filter radius r_{min} and a projection using
307 the threshold $\eta = 0.5$. This is done to ensure a well-
308 defined interface. The obtained variable $\hat{\xi}$ is re-filtered
309 using the erosion radius r_e , leading to the re-filtered
310 variable $\hat{\tilde{\xi}}$. Finally, the re-filtered variable $\hat{\tilde{\xi}}$ is projected
311 at a low and a high threshold, $\{\underline{\eta}, \bar{\eta}\} = 0.5 \pm \Delta\eta$, yield-
312 ing intermediate variables $\hat{\tilde{\xi}}_1$ and $\hat{\tilde{\xi}}_2$, respectively. The
313 eroded and dilated variables, indicate which physical
314 phase is applicable in each element (where the dilated
315 variable, $\hat{\tilde{\xi}}_1$ is mapped for consistency):

$$\begin{cases} \text{Fluid 1:} & \xi_1 = 1 - \hat{\tilde{\xi}}_1 = 1 \\ \text{Fluid 2:} & \xi_2 = \hat{\tilde{\xi}}_2 = 1 \\ \text{Solid:} & \xi_1 = \xi_2 = 0 \end{cases} \quad (19)$$

316 Two advantages of the erosion-dilatation technique
317 should be mentioned here, one is that a separating solid
318 phase is guaranteed between the two fluids and the other
319 is that the thickness of this solid phase can be controlled.
320 A derivation of the required parameters to achieve a
321 given wall thickness w_e can be found in [6]. The deriva-
322 tion is based on solving the filtration and sharp projec-
323 tion steps analytically, which results in the following re-
324 lation:

$$\Delta\eta = 0.45 \Rightarrow r_e \approx 0.75w_e \quad (20)$$

325 It is noted that the first filtering operation should have a
326 filter radius larger than the wall thickness:

$$r_{min} > w_e \quad (21)$$

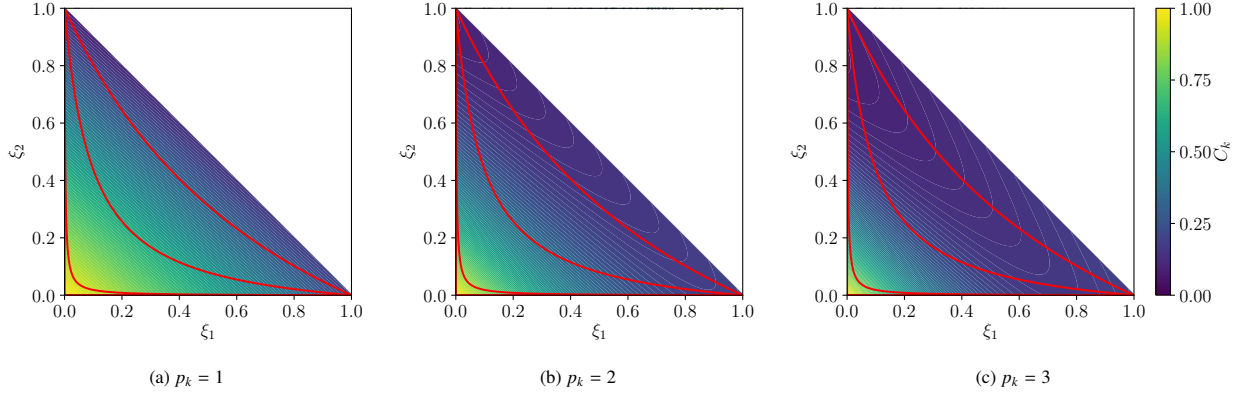


Figure 4: Interpolation function for the relative conductivity, with $C_k^1 = 0.2$ and $C_k^2 = 0.1$. The red lines show the ξ_1 and ξ_2 combinations obtained with the identification method for $\beta = \{1, 2, 4\}$. Note that the northeastern part is white, as the corresponding combinations between ξ_1 and ξ_2 are not feasible.

5.4. Interpolation functions

The relaxation of the optimization problem introduces the need for interpolation functions. Two parameters, the impermeabilities of both fluids α^γ and the conductivity ratio C_k are interpolated from the variables obtained by the erosion-dilation process seen in Figure 3.

The impermeabilities α^γ are interpolated from the corresponding variable from the erosion-dilation process ξ_γ . The interpolation is done using RAMP [10, 44, 45]:

$$\alpha^\gamma(\xi_\gamma) = \bar{\alpha}^\gamma \frac{1 - \xi_\gamma}{1 + \xi_\gamma q_\alpha} \quad (22)$$

where the upper limit $\bar{\alpha}^\gamma$ is the impermeability to be applied where the fluid γ is not present, as discussed in Section 3.1. The parameter q_α indicates the curvature of the function, which is linear when $q_\alpha = 0$.

The conductivity ratio C_k for the heat transfer problem is interpolated from both ξ_1 and ξ_2 . The interpolation has three bounds, such that Equation (8) is fulfilled. This is done by introducing the following interpolation function inspired by SIMP [46]:

$$C_k(\xi_1, \xi_2) = (1 - \xi_1 - \xi_2)^{p_k} + C_k^1 \xi_1 + C_k^2 \xi_2 \quad (23)$$

It is seen that the introduced interpolation function for C_k has a penalization power p_k on the solid phase, but not on the two terms corresponding to the fluid phases. Numerical studies concluded that this formulation circumvents high relative conductivities, when both ξ_1 and ξ_2 have intermediate values. In Figure 4, the interpolation function is shown for different penalization powers p_k .

5.5. Sensitivity analysis

The sensitivities of the objective and constraint functions are determined using the adjoint method. The method consists of setting up a Lagrangian function, where the residuals of the FEM problems are multiplied with the Lagrangian multipliers λ_i (also known as the adjoint variables):

$$\mathcal{L} = \Phi + \lambda_{F1}^T \mathbf{R}_{F1} + \lambda_{F2}^T \mathbf{R}_{F2} + \lambda_T^T \mathbf{R}_T \quad (24)$$

The derivative of the Lagrangian function is derived and rewritten using the chainrule, as seen in Appendix B.1, which results in the following sensitivity expression:

$$\frac{d\Phi}{d\xi} = \frac{\partial\Phi}{\partial\xi} + \lambda_T^T \frac{\partial\mathbf{R}_T}{\partial\xi} + \lambda_{F1}^T \frac{\partial\mathbf{R}_{F1}}{\partial\xi} + \lambda_{F2}^T \frac{\partial\mathbf{R}_{F2}}{\partial\xi} \quad (25)$$

where the Lagrangian multipliers are found by solving the three weakly coupled adjoint problems:

$$\left(\frac{\partial\mathbf{R}_T}{\partial T}\right)^T \lambda_T = \left(-\frac{\partial\Phi}{\partial T}\right)^T \quad (26)$$

$$\left(\frac{\partial\mathbf{R}_{F1}}{\partial \mathbf{u}_1}\right)^T \lambda_{F1} = -\left[\left(\frac{\partial\Phi}{\partial \mathbf{u}_1}\right)^T + \left(\frac{\partial\mathbf{R}_T}{\partial \mathbf{u}_1}\right)^T \lambda_T\right] \quad (27)$$

$$\left(\frac{\partial\mathbf{R}_{F2}}{\partial \mathbf{u}_2}\right)^T \lambda_{F2} = -\left[\left(\frac{\partial\Phi}{\partial \mathbf{u}_2}\right)^T + \left(\frac{\partial\mathbf{R}_T}{\partial \mathbf{u}_2}\right)^T \lambda_T\right] \quad (28)$$

The transposed tangential system matrices used in the adjoint problem are, as in the physical problem, adjusted for the imposed Dirichlet boundary conditions on the physical problem. However, it should be noted, that all Dirichlet boundary conditions in the adjoint problems are homogeneous.

5.6. Parameter continuation

The values of the projection sharpness, β , as well as the parameters of the interpolation functions, q_α and p_k in (22) and (23), respectively, are to be set in order to obtain physical interpolation schemes. The initial parameters are chosen to give the optimizer a lot of freedom in the beginning, and are then modified to obtain sharper interfaces and a more accurate physical modelling as optimization progresses. A way to avoid this continuation strategy would be to start with the final value and to tighten the asymptotes used in MMA [47]. For this approach to work, the initial design variable field must be at a value ensuring non-zero gradients of the projection function. However, for the present problem with multiple projections, the overlapping areas of non-zero sensitivities become non-existent for high β values [48].

For two- and three-dimensional problems, a continuation step is applied every 40th and 20th design iteration, respectively, if the constraints have been met in the previous 3 iterations. Numerical studies showed that taking a single relaxation step on q_α performed well. When increasing the projection sharpens, the β value is doubled. Finally, the penalization power for the relative conductivity interpolation, p_k , is increased simultaneously with the projection sharpness. The continuation scheme is shown in detail in Table 1. When starting with a higher

Table 1: Projection sharpness and interpolation parameters as function of continuation step. Step 1 is the initial setting.

Step	1	2	3	4	5	6	7
β	1	2	2	4	8	16	32
q_α	10^4	10^4	10^3	10^3	10^3	10^3	10^3
p_k	1	1	1	2	2	3	3

projection sharpness than $\beta = 1$, the scheme seen in Table 1 is used, replacing the β value in step 1 and omitting the obsolete continuation steps.

6. Results

First, a simple optimization problem in two dimensions is considered. This relatively simple problem allows for a demonstration and verification of the methodology and the design representation by one design variable. Thereafter, a more complex three-dimensional problem is considered, where the full potential of the method is demonstrated.

6.1. Two-dimensional counter-flow heat exchanger

6.1.1. Problem definition

The first case considered is a two-dimensional counter-flow heat exchanger. The setup is seen in Fig-

Table 2: Computational parameters of heat exchanger

Property	Cooled	Coolant
Reynolds number $Re[-]$	100	100
Solid Peclet number $Pe_s[-]$	4	4
Conductivity ratio $C_k[-]$	0.04	0.04
Impermeability $\bar{\alpha}[-]$	10^4	10^4

ure 5 and consists of a hot fluid inlet in the lower-left part of the domain, with the corresponding outlet on the opposite lower-right side of the domain. A cold fluid inlet is located at the upper-right side of the domain, with the corresponding outlet at the opposite upper-left side. The inlets have parabolic velocity profiles assuming fully-developed laminar flow. Homogeneous Dirichlet boundary conditions are applied on the pressures at the respective outlets. Furthermore, a straight out velocity boundary condition is placed on the velocities at the outlets. The areas near the in- and outlets are excluded from the optimization to ensure undisturbed in- and outflow.

The problem presented here is optimized for computational Reynolds number $Re_{comp}^\gamma = 100$, which leads to an actual Reynolds number $Re^\gamma = 46$, for both fluids, when adjusted for their respective inlet sizes [24]. The reference velocity, U , is the maximum velocity, located at the center of the inlets. The computational Peclet number is $Pe_{comp}^\gamma = 100$, as for the Reynolds numbers, this leads to the actual Peclet number $Pe^\gamma = 46$. The computational non-dimensional parameters are seen in Table 2. The optimization process is cut-off after a maximum of 500 design iterations.

The optimization problem is run with different maximum pressure drop constraints, which are obtained from the empty straight-channel design, as seen in Figure 6. The objective function is compared to the one from the same baseline design:

$$\Delta P_{base}^\gamma = 1.57 \quad \Phi_{coolant, base} = 0.856 \quad (29)$$

6.1.2. Results

The problem is optimized for a range of values of admissible pressure drops ΔP_{max} . It should be noted that the pressure drop in the channels cannot be smaller than the one from the baseline design, where the two channels are straight and parallel in the entire domain. The domain consists of $324 \times 72 \times 1$ cubic elements. The filter radii are set, such that the wall is $w_e = 0.075$ thick, corresponding to ≈ 5 elements. Furthermore, the filter radius has been set to $r_{min} = 0.08$, as discussed in Section 5.3.

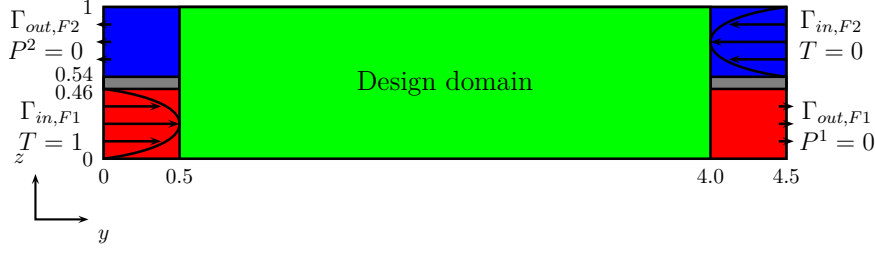


Figure 5: Sketch of the design domain for the two dimensional counter-flow heat exchanger. Green indicates the actual design domain, passive domains of the coolant- and cooled fluids are shown in blue and red, respectively. Grey indicates passive solid domains. The reference length is the height of the domain, $L = 1$ and the reference velocity, the velocity at the inlet center, $U^y = 1$.

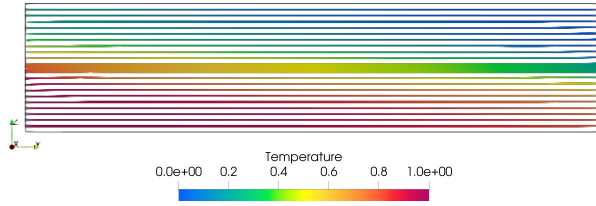


Figure 6: Baseline design of the two-dimensional counter-flow example. The two fluid phases consist of straight channels separated by a wall. Structure and streamlines are colored by temperature.

479 (NTU) [49]:

$$\epsilon = \frac{\Phi_{coolant}}{\Phi_{coolant, max}} = \frac{NTU}{1 + NTU} \quad (30)$$

$$NTU = \frac{UA}{c_p \dot{m}} \quad (31)$$

480 where $\Phi_{coolant, max}$ is the theoretical maximum heat transfer and UA the overall heat transfer coefficient, which is dependent of the heat transfer coefficients $h_{F\gamma}$ of the two fluids:

$$UA = \left(\frac{L_w}{k_w A} + \frac{1}{h_{F1} A} + \frac{1}{h_{F2} A} \right)^{-1} \quad (32)$$

$$h_{F\gamma} = \frac{Nu_\gamma k_{F\gamma}}{D_h} \quad (33)$$

484 where Nu_γ is the Nusselt number, $k_{F\gamma}$ the conductivity of the respective fluid and L_w the thickness of the solid wall. The Nusselt number for both fluids is found to be $Nu = 6.1$ for this counter-flow heat exchanger problem. This was done by performing a numerical analysis of the baseline model in COMSOL. The hydraulic diameter is twice the height of the infinitely wide channel, $D_h = 2w$, where w is the channel height. In the presented 2D case, the heat transfer area A is equal to the length of the heat exchanger. Assuming all the pressure loss goes to making the channels narrower and that the flow is always fully developed, the width of the channel can be computed from integrating the volume flux of the Poiseuille flow:

$$V = \int_0^w -\frac{1}{2\mu} \frac{dP}{dy} (zw - z^2) dz \quad (34)$$

$$\Rightarrow w = w_{base} \sqrt[3]{\frac{\Delta P_{base}}{\Delta P}}$$

488 Combining Equations (30-34), an analytical heat transfer enhancement for straight pipes with varying channel width w can be computed and compared to the optimized designs. This is done assuming that the two fluids behave equally and that the allowable pressure drop

454 Two initial designs are considered in this example.
455 The first one consists of the two parallel channels. In the
456 second initial design, the entire design domain has been
457 set to an intermediate design variable value, $\xi = 0.5$,
458 violating the strict separation of fluids.

459 A selection of the optimized structures, obtained at
460 different admissible pressure drops and using the two
461 initial designs are seen in Figure 7. With both initial de-
462 signs, the channels get narrower, as the admissible pres-
463 sure drop is increased. The narrower channels increase
464 the flow speed of both fluids, which increases the heat
465 transfer coefficient. Furthermore, in some cases, it is
466 seen that the channels bend towards the domain bound-
467 ary. A reason for this might be that a solid wall, with a
468 high conductivity, can be avoided along the fluid. This
469 wall might otherwise act as an unwanted regenerator.

470 In Figure 7, a higher heat transfer is also observed for
471 the designs optimized with a higher admissible pressure
472 loss. In Figure 8, the heat transfer improvements (rela-
473 tive to the baseline design and to a theoretical limit) are
474 compared for different admissible pressure drops (rela-
475 tive to the baseline design). The monitored improve-
476 ment can be compared to a function of the admissible
477 pressure drop ΔP_{max} . This is done by noting the effec-
478 tiveness ϵ as a function of the Number of Transfer Units

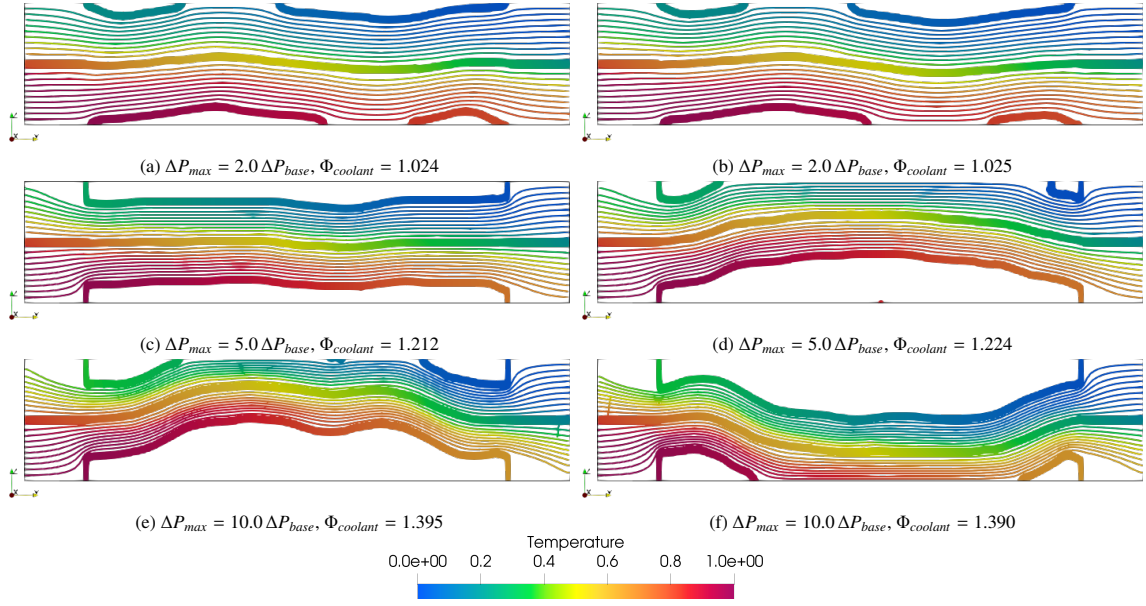


Figure 7: Optimized structures and corresponding streamlines, colored by temperature. The structures are optimized with two different initial designs being, (a, c, e) the parallel channels and (b, d, f) $\xi = 0.5$. The designs are optimized for different admissible pressure drops, (a, b) $\Delta P_{max} = 2.0 \Delta P_{base}$, (c, d) $\Delta P_{max} = 5.0 \Delta P_{base}$ and (e, f) $\Delta P_{max} = 10.0 \Delta P_{base}$. Structures are thresholded at $\alpha^1 > 0.1\bar{\alpha}^1 \wedge \alpha^2 > 0.1\bar{\alpha}^2$.

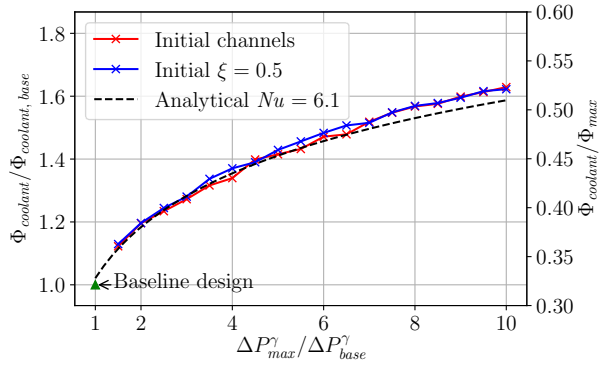


Figure 8: Improvement and fit of the transferred heat as a function of the admissible pressure drop in the fluids.

is used exclusively to make the channels thinner on the entire length of the domain.

From Figure 8, it is seen that there is a very nice correspondence between the performance of the optimized designs and the theoretical prediction. At larger admissible pressure drops, the optimized designs outperform the theoretical prediction marginally. This confirms that, at least for this example, it is possible to obtain close to optimal designs using the presented methodology. The higher heat transfer by the designs obtained using the present methodology is due to the larger design freedom, which, for instance, makes the channels slightly curved. The slight advantage of these features

can be seen from the two designs optimized for $\Delta P_{max} = 5 \Delta P_{base}$, where the design with the curved feature, Figure 7d, slightly outperforms ($\sim 1\%$) the designs, where the channels have been narrowed, but stayed parallel, Figure 7c.

Figure 9 shows the design field ξ and the intermediate fields, obtained by optimizing with an admissible pressure drop $\Delta P_{max} = 5 \Delta P_{base}$ with the parallel channel initial design. From the eroded and dilated design fields, ξ_1 and ξ_2 , seen in Figures 9c and 9d, it is seen that the fields have the same features, but that they are eroded and dilated versions of Figure 9b, which results in the wall. It is observed that the islands at the top and bottom of the computational domain are of the opposite fluid. This is also seen in Figure 10, where the fluid domains are shown for the optimized heat exchanger design. In Figure 9g, the relative conductivity, C_k , in the design domain is shown. The walls are clearly identified with the higher conductivity. At the transition between the solid and the fluid, some few elements of intermediate conductivities are observed. However, this has very small influence on the final design, as very few elements are concerned.

In order to illustrate the distribution of the physical fields α^γ and C_k along with their effect on the velocities and temperature, these quantities are probed along the vertical centerline in the baseline design seen in Figure 6 and in the design optimized with the baseline used as

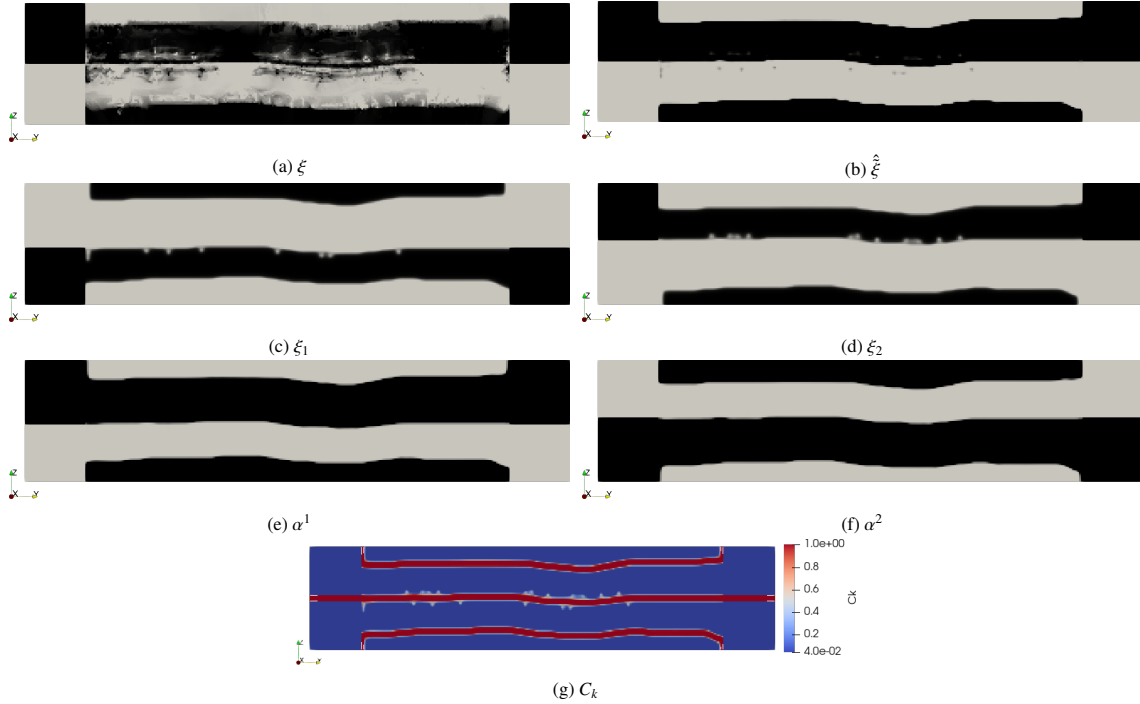


Figure 9: Optimized fields, obtained by optimizing the parallel channels initial design, with a $\Delta P_{max} = 5.0 \Delta P_{base}$ pressure drop constraint. The design field ξ (a) is filtered and projected to the filtered and projected field $\hat{\xi}$ (b). The erosion-dilation process, discussed in Section 5.3, is then used to generate ξ_1 (c) and ξ_2 (d), where the black region indicates the presence of the respective fluid. These fields lead to the physical fields (e-g), interpolated as discussed in Section 5.4.

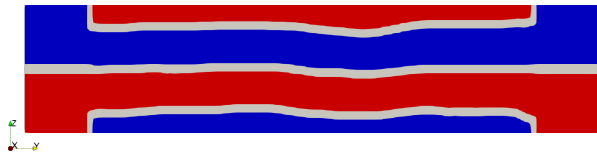


Figure 10: Overview of the fluid domains in the design optimized for $\Delta P_{max} = 5.0 \Delta P_{base}$, with the parallel channels initial design. Red color denotes fluid 1, blue color fluid 2, and white the solid interface separating the two fluids.

544 initial design and $\Delta P_{max} = 5 \Delta P_{base}$, seen in Figure 7c.
 545 The probes are seen in Figure 11. In both cases, the
 546 wall is identified by the high relative conductivity and
 547 impermeabilities, as well as the low temperature gradi-
 548 ent, caused by the high conductivities in the wall. In the
 549 probe of the optimized design, Figure 11b, the *islands*
 550 of fluid are again highlighted. They seem to act as heat
 551 reservoirs. The flow of both fluids is seen to be present
 552 in the corresponding main fluid domain (no flow in the
 553 islands).

554 The optimization history of the design with $\Delta P_{max} =$
 555 $5 \Delta P_{base}$ and starting with $\xi = 0.5$, is seen in Figure
 556 12. Here it is seen that the objective function is very
 557 low, near the theoretical maximum, in the early design

558 iterations. The continuation steps are clearly identified,
 559 where spikes appear in the constraint function values
 560 and where the objective function value rises. The three
 561 shown preliminary designs from just prior to the contin-
 562 uation steps clearly illustrate that the two fluids are able
 563 to mix, when the projection value is low. This is due to
 564 the combination of the identification method discussed
 565 in Section 5.3 and the porous formulation. It is hence
 566 seen (from the first history state, where the streamlines
 567 mix) that the pressure constraint does not really have an
 568 influence before the continuation step to $\beta = 4$, as the
 569 flow is mostly porous prior to this point.

570 A study on a refined mesh for the cases with $\Delta P_{max} =$
 571 $5 \Delta P_{base}$ can be seen in Appendix C. Although obtained
 572 topologies change slightly, the objective values are
 573 found to change insignificantly with mesh-refinement.

574 6.2. Three-dimensional shell-and-tube heat exchanger

575 6.2.1. Problem definition

576 The second considered case is inspired by a shell-
 577 and-tube heat exchanger design. Figure 13 shows the
 578 design problem. The heat exchanger has circular in-
 579 and outlets of the coolant on one face and circular in-
 580 and outlets of the cooled fluid on an adjacent face. Both

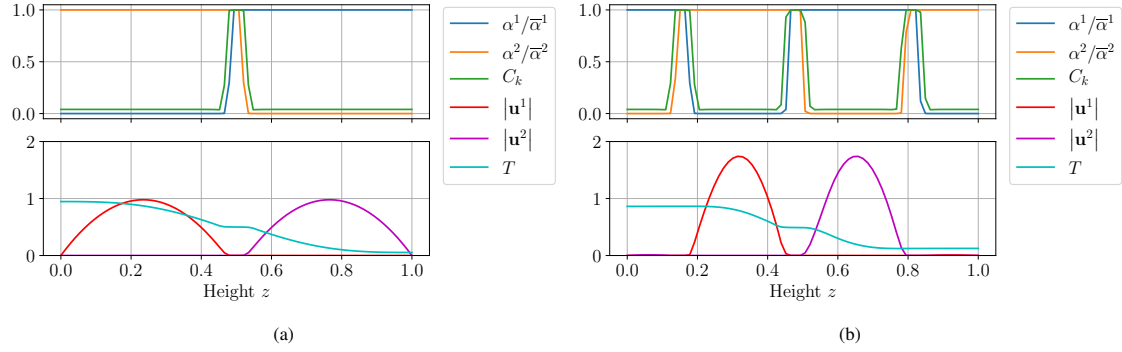


Figure 11: Probes showing physical quantities, velocity magnitudes and temperatures along the vertical centerline in the (a) baseline design and (b) design optimized with the initial channels and $\Delta P_{max} = 5 \Delta P_{base}$.

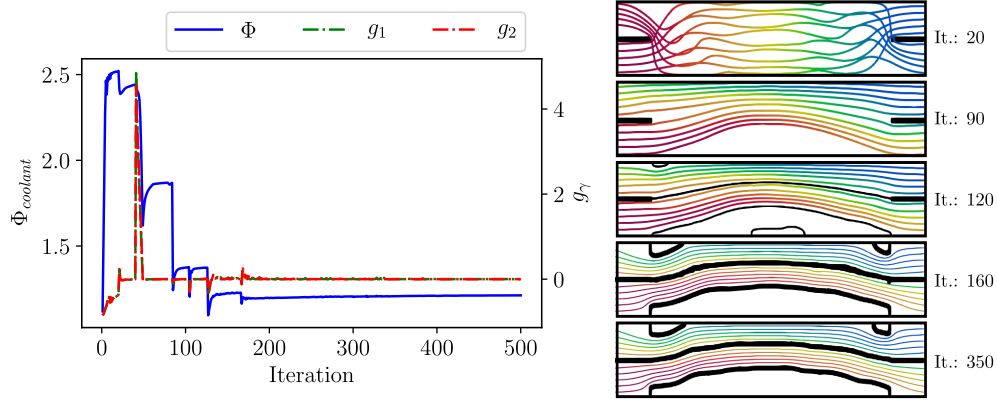


Figure 12: Objective- and constraint function, $\Phi_{coolant}$ and g_γ , respectively, history over design iterations for the optimization with the initial channel design and $\Delta P_{max} = 5 \Delta P_{base}$. Early design iterations, with low projection sharpness, show that no interface is formed and fluids are not well separated. As the continuation progresses, fluids get more separated, and finally, an interface is formed.

581 inlet velocity profiles are assumed to be parabolic with
 582 respect to radial distance. The size of the heat exchanger
 583 is inspired by Ozden and Tari [50].

584 Based on the information, presented in Table 3, the
 585 Reynolds- and Peclet numbers of both the cooled and
 586 coolant phase can be computed. The solid material is
 587 set to be stainless steel, the hot fluid to be oil and the
 588 coolant to be water. The Reynolds and solid Peclet num-
 589 bers seen in Table 3 are both converted to their computa-
 590 tional equivalents, adjusting for the non-dimensional in-
 591 let diameters [24]. The Darcy number is set to $Da = 10^8$
 592 to limit the porous flow. The final computational param-
 593 eters are shown in Table 4.

594 The optimization is carried out on the half domain,
 595 as depicted by the $z = 0.5$ plane in Figure 13. The
 596 boundary conditions on this plane are of symmetric
 597 type, with no-through flux of mass and heat. This sym-
 598 metric boundary condition constrains the obtained des-
 599 igns to be symmetric. The design domain is discretized
 600 by $(120 \times 400 \times 60)$ elements. The filter radii are set to

Table 3: Parameters of heat exchanger

Property	Cooled side	Coolant side
	Oil, 1	Water, 2
Mass flow \dot{m} [kg·s ⁻¹]	$4.57 \cdot 10^{-3}$	$9.64 \cdot 10^{-4}$
Inlet temperature T [C]	90	65
Density ρ [kg·m ⁻³]	866.4	980
Dynamic viscosity μ [N·s·m ⁻²]	0.0215	$4.32 \cdot 10^{-4}$
Heat capacity c_p [J·kg ⁻¹ ·K ⁻¹]	2088	4188
Conductivity k [W·m ⁻¹ ·K ⁻¹]	0.1233	0.6
Solid conductivity k [W·m ⁻¹ ·K ⁻¹]	30	
Pressure drop Δp [Pa]	16402	3080
Reynolds number [-]	10.9	150
Peclet number [-]	3973	453

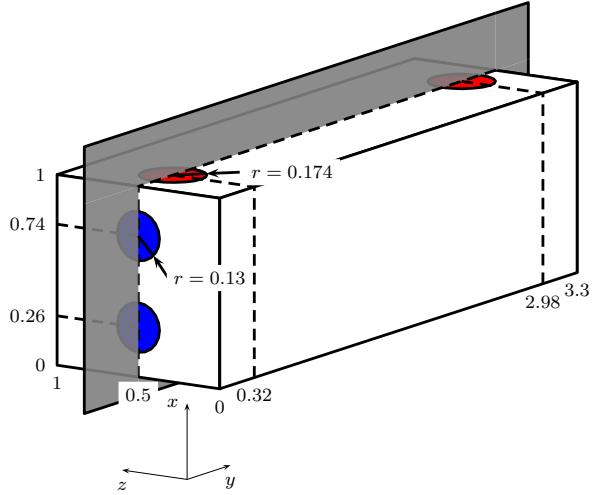


Figure 13: Design domain of the considered heat exchanger. The in- and outlets of the coolant, water, are located on the y -min plane (in blue) and the in- and outlets of the cooled fluid, oil, are located on the x -max plane (in red). The grey plane is the symmetry plane located at $z = 0.5$. The reference length is the height of the heat exchanger, $L = 146 \cdot 10^{-3}$ [m].

Table 4: Computational parameters of the three dimensional heat exchanger optimization problem.

Property	Cooled	Coolant
Reynolds number $Re[-]$	31.32	578
Solid Peclet number $Pe_s[-]$	46.92	34.8
Conductivity ratio $c_k[-]$	$4.11 \cdot 10^{-3}$	0.02
Impermeability $\bar{\alpha}[-]$	$3.19 \cdot 10^6$	$1.73 \cdot 10^5$

601 $r_{min} = 0.07$ and $r_e = 0.035$, respectively, resulting in a
602 minimum wall thickness of $w_e = 0.0467$, correspond-
603 ing to ≈ 5.6 elements. The computational cost of the
604 optimization process is between 7 and 15 hours on 320
605 AMD EPYC 7351 CPU cores. The large span may be
606 due to the network topology of the cluster and to the
607 ramping scheme on the Reynolds number in the non lin-
608 ear Navier Stokes solver.

609 Two baseline designs are considered, both inspired
610 by shell-and-tube heat exchangers. In both cases, the
611 coolant fluid is the tube side. The coolant fluid flows
612 through one or four tubes (respectively half and two
613 tubes in the half domain), in the two baseline designs
614 seen in Figure 14, respectively. Near the plane with
615 the coolant inlet and outlet, a manifold is located which
616 redirects the coolant fluid and a small wall separates the
617 coolant in- and outlet manifolds.

618 The baseline designs have different pressure drops
and heat transfers, seen in Table 5. The baseline de-

Table 5: Comparison of performance of the two baseline designs.

Design	ΔP_{base}^1	ΔP_{base}^2	$\Phi_{coolant, base}$
1 tube	11.9	3.56	4.68
4 tubes	57.4	3.08	7.27

619 signs are optimized with their corresponding pressure
620 drops, i.e. $\Delta P_{max}^y = \Delta P_{base}^y$. For each baseline pressure
621 drop, four initial designs are considered: One where the
622 design variable is uniform $\xi = 0.5$ in the design do-
623 main, and three where the respective baseline design is
624 utilized, but subjected to different projection sharpness,
625 $\beta_{initial} = \{1, 4, 8\}$. In all cases, the optimization is cut-
626 off after 350 design iterations. The higher initial β val-
627 ues ensures more well-defined and impermeable walls.
628 This enables the the coolant flow to travel through the
629 initial tubes, reaching deeper into the domain in the
630 early design iterations. However, for lower β values
631 and the uniform distribution of $\xi = 0.5$, the walls are ei-
632 ther fairly porous or non-existent. This means that the
633 coolant will take the path of least resistance, which is di-
634 rectly from inlet to outlet and not reaching deep into the
635 computational domain. Having the flow fields reaching
636 far into the design domain yields a wider range of spa-
637 tial sensitivity information. Hence, the flow field in the
638 initial design, and the early design iterations, has a very
639 high impact on the final design and will vary depending
640 on the given problem and boundary conditions.

642 6.2.2. Results

643 With both baseline designs, seen in Figure 14, the
644 heat exchanger is optimized using the respective ini-

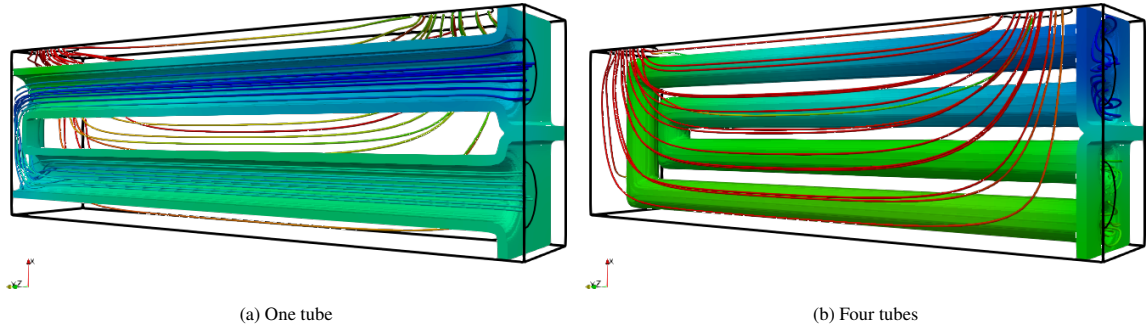


Figure 14: Half baseline designs, with the symmetry plane depicted in Figure 13. Structures and streamlines are colored by temperature, in- and outlets highlighted with black contours, and structure thresholded at $\alpha^1 > 0.1\bar{\alpha}^1 \wedge \alpha^2 > 0.1\bar{\alpha}^2$.

645 tial baseline designs and β values, as previously discussed. All designs are optimized with the maximum pressure drop being equal to the pressure drop in its respective baseline design. In total, eight optimized designs are obtained and the solid structures with streamlines of the designs are seen in Figure 15³. For the designs optimized from a loosely-defined initial design ($\beta_{initial} = 1$), seen in Figures 15a-15d, the coolant channels do not reach the end of the design domain. However, as seen in Figures 15e-15h, when starting from more well-defined initial designs (higher $\beta_{initial}$), the coolant channels reach further into the design domain,

657 On the obtained solid structures, microvilli-like extended features are observed, going into the cooled fluid domain seemingly normal from the coolant tube surface. Microvilli are biological features, which are a part of the cellular membrane, increasing the surface area for absorption and other processes, but holding the volume increase to a minimum. The microvilli-like features from the different tubes are shifted in positions, as seen in the closeup from Figure 16 (from the design seen in Figure 15f, optimized with $\beta_{initial} = 4$ and the four channel baseline initial design field). It is seen that the microvilli-like features are placed in shifted positions relative to each other, such that the flow passes them in a curved manner, which increases the surface area, with flow next to it.

672 Figure 17 shows the flow of the tube side coolant. It is again observed that starting with an initial design, where the coolant flow reaches the back of the domain, results in designs, where the coolant channels are present in the entirety of the domain. However, for the designs where the coolant flow did not reach far into the computational domain, Figures 17a-17d, it is seen that the back of the

679 domain is almost unused, as neither structures nor visible temperature variations are present in these areas. The entirety of the design domain is hence not fully exploited when starting with a too poorly-defined and permeable initial design. On the other hand, when a higher initial projection sharpness is used, the topology of the initial design of the coolant fluid is preserved to a certain extent, as shown in Figures 17e-17h. The designs obtained with $\beta_{initial} > 1$ and the one channel baseline design, seen in Figures 15e, 15g, 17e and 17g, have a topology similar to the one seen in the baseline, Figure 14a. The coolant channels are, for the most part, attached to the symmetry plane. The upper channel of the design optimized with $\beta_{initial} = 4$ is detached from the symmetry plane for a little distance. This increases the contact surface between the fluids and the solid, but probably also has an influence on the heat transfer coefficient.

697 When using the baseline design with four channels, Figure 14b, and $\beta_{initial} > 1$, the optimized designs seen in Figures 15f, 15h, 17f and 17h, have coolant fluid domain topologies, that also are preserved to a certain extent. The coolant fluid channel paths are, however, modified significantly in comparison to the baseline design. This also affects the flow of the cooled fluid, which the optimized structure disturbs more than what is observed in the baseline design. This higher disturbance of the cooled flow probably also is of benefit to the heat transfer.

708 Table 6 shows the obtained heat transfer in the different optimized designs. All optimized designs perform better, than both baselines, whose heat transfers also are seen in Table 6. The relative improvements, compared to the better four-channel baseline, range from 74.8% (starting from $\beta_{initial} = 1$, $\xi = 0.5$ and using one channel design pressure drops) to 113% (starting from $\beta_{initial} = 4$ with the four channel baseline). Furthermore,

³Animations of the obtained structures can be found in the supplementary material.

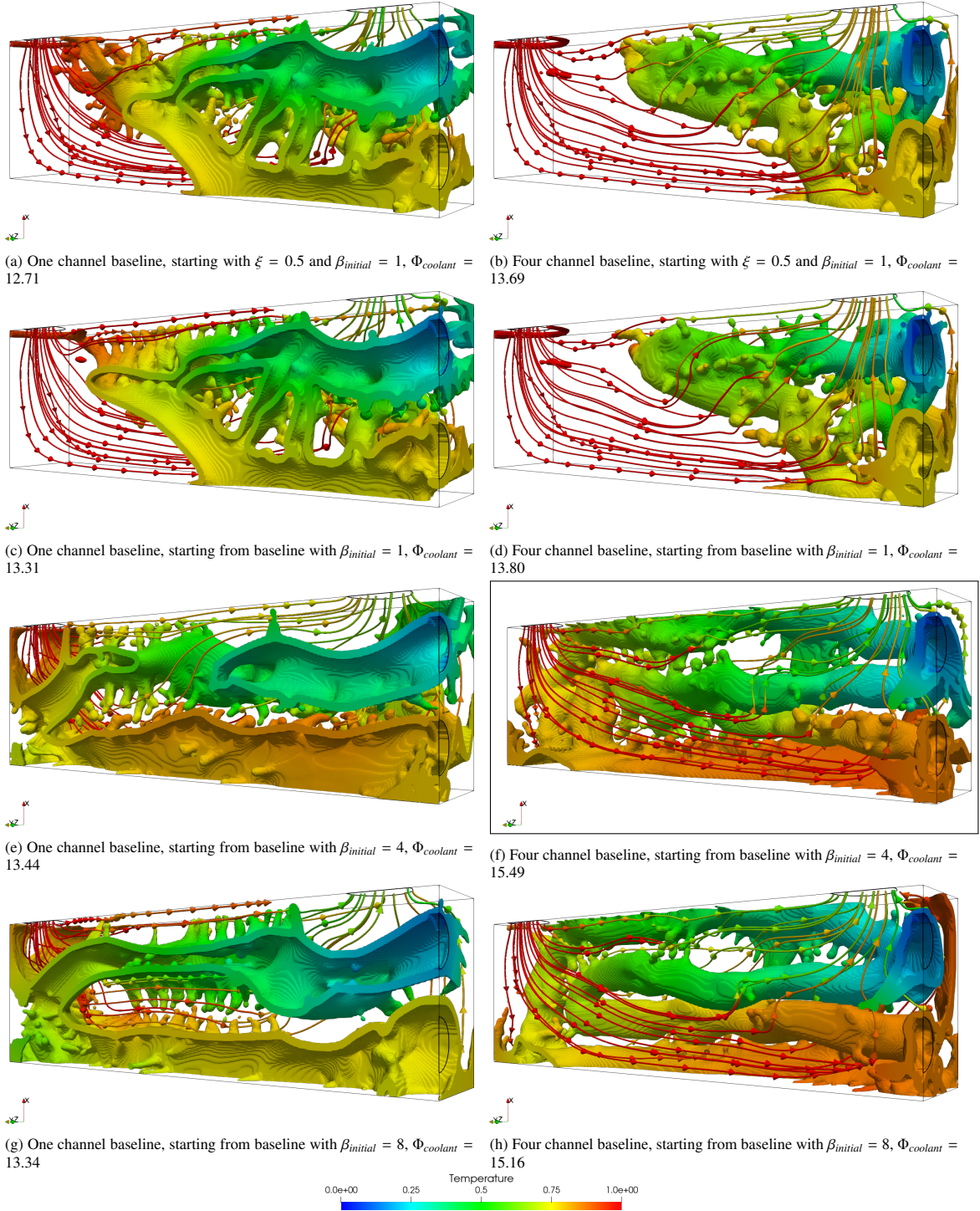


Figure 15: Optimized structures, and corresponding streamlines of the cooled fluid, both colored by temperature. The structures are thresholded at $\alpha^1 > 0.1\bar{\alpha}^1 \wedge \alpha^2 > 0.1\bar{\alpha}^2$.

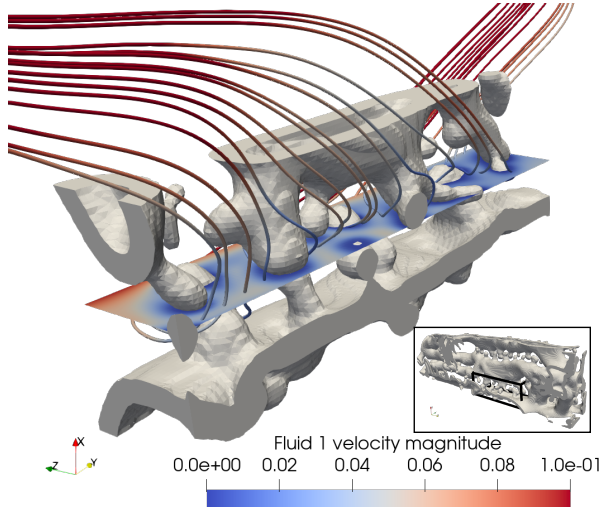


Figure 16: Cut of the solid structure of the design optimized with the four channel baseline, with the initial projection sharpness $\beta_{initial} = 4$. The velocity magnitude of the cooled fluid 2 is seen on the plane.

716 with both baseline designs, it is seen that the designs opt-
717 imized with the initial projection sharpness $\beta_{initial} = 4$
are the ones performing best. Redimensionalizing the

Table 6: Comparison of the thermal energy flux out of the cold fluid. It is seen that there, in all cases, is a considerable improvement of the baseline design. The designs optimized with the four-channels baseline design always perform better. Furthermore, with both baseline designs, starting with $\beta = 4$ yields the best design.

		1 channel	4 channels
Baseline design		4.68	7.27
Optimized	$\xi_{initial} = 0.5, \beta_{initial} = 1$	12.71	13.69
	$\beta_{initial} = 1$	13.31	13.80
	$\beta_{initial} = 4$	13.44	15.49
	$\beta_{initial} = 8$	13.34	15.16

718 best optimized design, the transferred thermal power is
719 obtained, to be $P = 89.9$ W. Likewise, the best base-
720 line (four channels), has a transferred thermal power of
721 $P = 42.2$ W.
722

723 To investigate the influence of the solid conductiv-
724 ity on the obtained design, the optimization is rerun for
725 the case where the solid conductivity is set such that
726 $k_s = k_{coolant}$, where $k_{coolant}$ is the conductivity of the
727 coolant fluid 2, seen in Table 3. This leads to the com-
728 putational parameters seen in Table 7. The optimization
729 is run using the four-channel baseline design, and the
730 initial projection sharpness $\beta_{initial} = 4$, which produces
731 the best results.

732 The obtained design is seen in Figure 18. As one
733 would expect, the microvillies are not present in the

Table 7: Computational parameters of the three dimensional heat exchanger optimization problem, with $k_s = k_{coolant}$.

Property	Cooled	Coolant
Reynolds number $Re[-]$	31.32	578
Solid Peclet number $Pe_s[-]$	2346	1740
Conductivity ratio $C_k[-]$	0.2055	1
Impermeability $\bar{\alpha}[-]$	$3.19 \cdot 10^6$	$1.73 \cdot 10^5$

734 design, as the higher solid surface area is not an ad-
735 vantage in this case and significantly less heat can be
736 conducted through the microvillies. However, other in-
737 teresting features, such as a serpentine channel can be
738 observed in the obtained design. This serpentine chan-
739 nel also increases the surface area. However, with the
740 serpentine feature, the heat transfer is more convection
741 dominated near the wall.

742 To confirm the result quality, the objective function
743 (14) is cross-checked with the original coolant solid
744 Peclet number (Table 4), which was $\Phi_{coolant} = 14.15$.
745 The performance of the design optimized using $k_s =$
746 $k_{coolant}$, is also evaluated using the original solid con-
747 ductivity parameters seen in Table 4. Conversely, the
748 design optimized with the parameters from Table 4, the
749 four-channel baseline design and $\beta_{initial} = 4$, seen in Fig-
750 ures 15f and 17f, is evaluated with the parameters corre-
751 sponding to the lower solid conductivity, seen in Table
752 7. From Table 8, it is seen that the obtained designs
753 clearly perform best for the physical conditions, which
they have been optimized for.

Table 8: Cross check of the best design optimized with the physical parameters from Table 4 (high solid conductivity) and with the ones from Table 7. The performances of the two designs are evaluated with the physical parameters from the other one, respectively. Note, that in all cases $\Phi_{coolant}$ is computed using the coolant solid Peclet number shown in Table 4.

		Evaluated	
		Tab. 4	Tab. 7
Optimized	Tab. 4	15.49	12.05
	Tab. 7	13.64	14.15

754 In order to demonstrate the influence of the wall
755 thickness, an optimization is run with the physical pa-
756 rameters from Table 4 and the filter radii $r_{min} = 0.1$
757 and $r_e = 0.05$, resulting in a minimum wall thickness
758 $w_e = 0.0667$, corresponding to ≈ 8 elements. The base-
759 line design used here is similar to the four-channel base-
760 line design seen in Figure 14b, where the internal diam-
761 eter of the tube side is conserved. However, the in- and
762 outlet manifolds on the tube side cannot be moved due
763 to the inlet locations, resulting in an increase in pres-

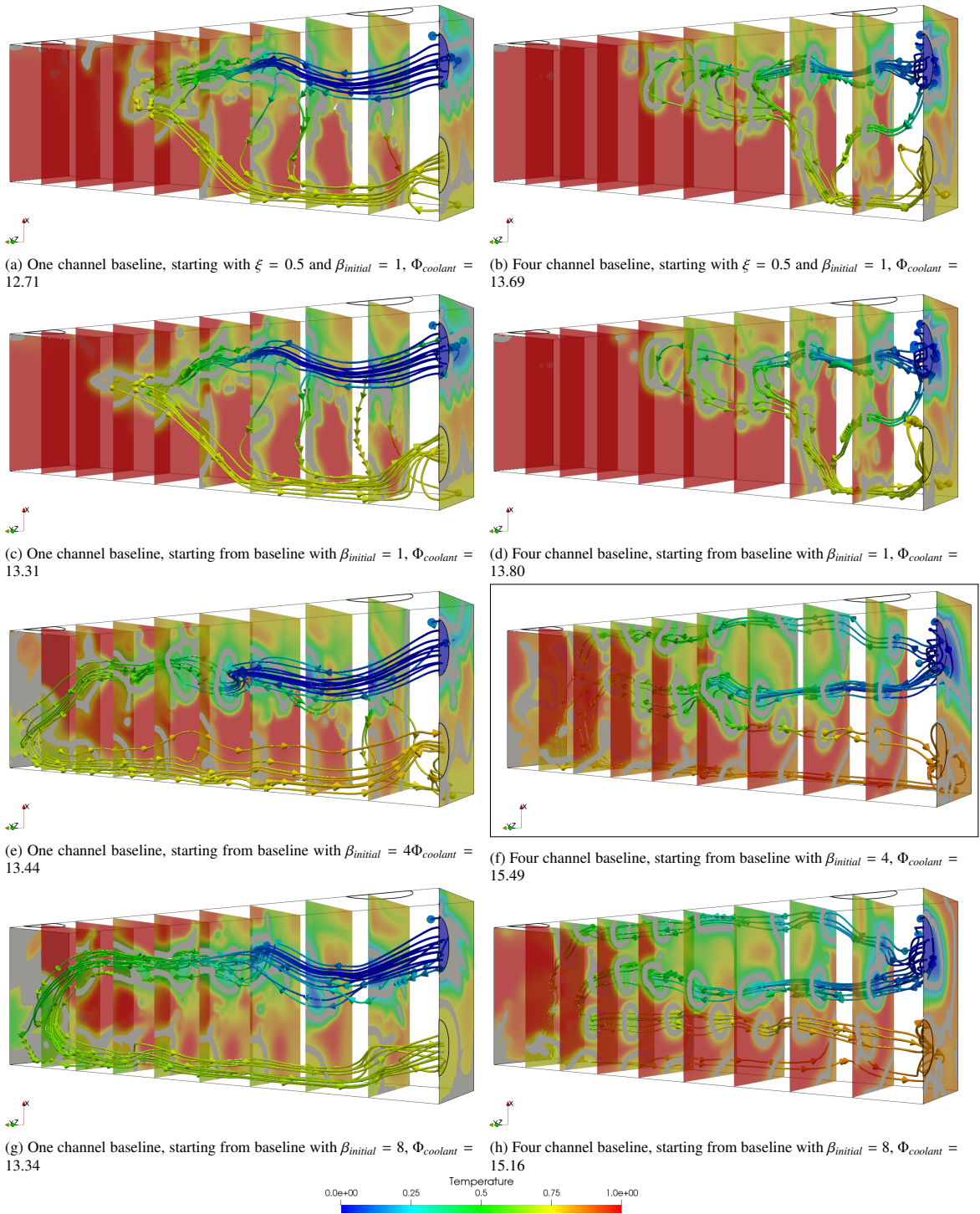


Figure 17: Streamlines of the coolant fluid and slices through the design domain. Slices and streamlines are colored by temperature. The structures (thresholded at $\alpha^1 > 0.1\bar{\alpha}^1 \wedge \alpha^2 > 0.1\bar{\alpha}^2$) on the slices are colored in grey.

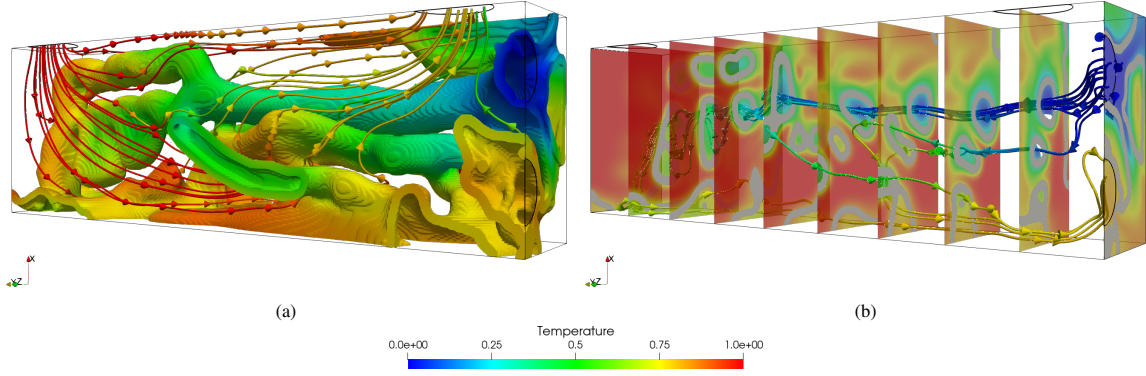


Figure 18: Design obtained with the solid conductivity set equal to the coolant conductivity. (a) shows the obtained structure with the cooled fluid streamlines and (b) slices of the domain with gray solid and coolant streamlines (in both cases the structure is thresholded at $\alpha^1 > 0.1\bar{\alpha}^1 \wedge \alpha^2 > 0.1\bar{\alpha}^2$).

765 sure drop. The pressure drops from the present baseline
 766 design are used for the constraints in the optimization
 767 process resulting in:

$$\Delta P_{max}^1 = 120.4 \quad \Delta P_{max}^2 = 6.1 \quad \Phi_{coolant, base} = 5.29 \quad (35)$$

768 Due to these higher pressure drop constraints, approx-
 769 imately twice the ones used previously (Table 5) the
 770 obtained objective function from this optimization is
 771 not directly comparable to the ones obtained previously.
 772 This study hence only investigates the influence of the
 773 wall thickness qualitatively, while a quantitative com-
 774 parison should bear the difference in the pressure drop
 775 constraints in mind. The lower objective function in the
 776 baseline design can be related to the higher wall thick-
 777 ness.

778 The obtained design is seen in Figure 19. Most
 779 microvilli-like features have disappeared due to the
 780 higher wall thickness. Some features observed in the
 781 design might point to the advantage of the microvillies,
 782 however, it seems that these features have not been able
 783 to develop into the shell side of the heat exchanger.

784 The objective function of the design optimized with
 785 the larger wall thickness is $\Phi_{coolant} = 14.97$. Taking the
 786 larger pressure drop constraints into consideration, it is
 787 clear, that the heat exchanger with the increased solid
 788 wall thickness has inferior performance.

789 In order to verify that the wall thickness is indeed
 790 controlled, as discussed in Section 5.3, the solid struc-
 791 ture from the best obtained result obtained with the
 792 small wall thickness, and from the structure with the
 793 high wall thickness are compared in Figure 20. Here
 794 it is seen that the wall thickness imposed through the

795 erosion-dilation filter radius, as described by equation
 796 (20), is satisfied in both cases. Some minor deviations
 797 might be observed due to the discretization and will dis-
 798 appear with mesh refinement.

799 7. Discussion and conclusion

800 In this paper, a new approach for topology optimiza-
 801 tion of two fluid heat exchangers is presented. The for-
 802 mulation, based on a single design variable field, guar-
 803 antees the presence of a solid interface between the two
 804 fluid phases based on an erosion-dilation identification
 805 method. The two mass transfer and one heat transfer
 806 problems are solved sequentially in the entirety of
 807 the design domain. The optimization maximizes the
 808 amount of transferred heat with maximum pressure drop
 809 constraints on both fluids. The methodology is applied
 810 to two numerical examples.

811 In the two-dimensional counter-flow example where
 812 the design freedom is limited, it is seen that the chan-
 813 nels are made narrower, as the allowable pressure drop
 814 is increased. This provides an excellent agreement be-
 815 tween the amount of transferred heat and the maximum
 816 allowable pressure drop obtained using Poiseuille flow
 817 and the $\epsilon - NTU$ method. This indicates that the im-
 818 provement in heat transfer, obtained with the topology
 819 optimization process introduced here, can be related to a
 820 theoretically derived optimum (for a "one-dimensional"
 821 optimization) - at least for this simple case.

822 In the three-dimensional example, simple shell-and-
 823 tube-like baseline designs were significantly enhanced,
 824 with up to a 113% improvement compared to the best-
 825 performing baseline. In the obtained results, the impor-
 826 tance of the flow field in the initial design was high-
 827 lighted. This relates to the computation of the sensi-

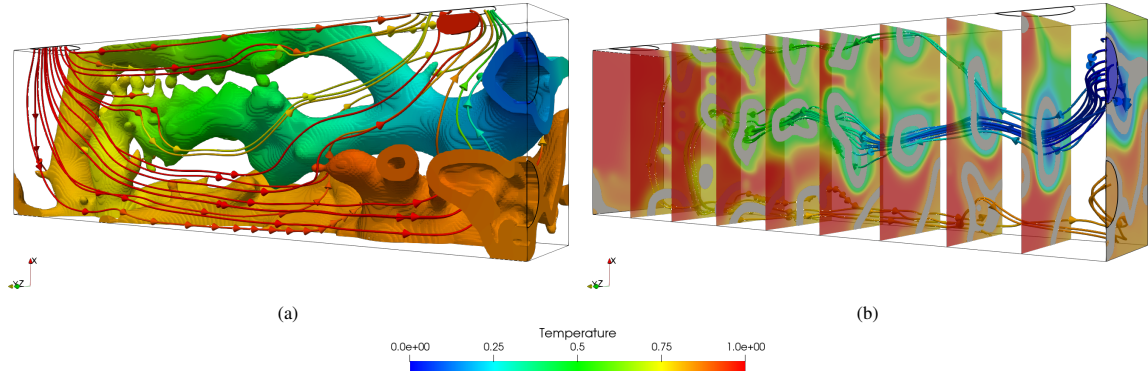


Figure 19: Design obtained with the higher filter radii $r_{min} = 0.1$ and $r_e = 0.05$, leading to the wall thickness $w_e = 0.0667$. (a) shows the obtained structure with the cooled fluid streamlines and (b) slices of the domain with gray solid and coolant streamlines (in both cases the structure is thresholded at $\alpha^1 > 0.1\bar{\alpha}^1 \wedge \alpha^2 > 0.1\bar{\alpha}^2$).

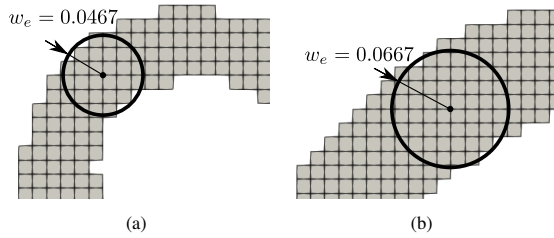


Figure 20: Slice of a solid wall feature of the design seen in (a) Figure 15f and (b) Figure 19 (right). The two thicknesses are seen to correspond to the thickness specified when determining the filter radii.

828 tivities in the early design iterations, which are crucial
 829 to the later optimization process. In the optimized des-
 830 signs, microvilli-like features are observed, which en-
 831 hance both the surface area, but also perturb the flow
 832 near them. The microvillies disappear with decreasing
 833 solid conductivity or increasing wall thickness.

834 The novel and intricate designs appearing when uti-
 835 lizing the presented methodology have been challeng-
 836 ing to export to a CAD-based engineering analysis en-
 837 vironment. More research into the transformation from
 838 density-based representations to CAD/spline basis are
 839 needed. In order to evaluate the performance of the ob-
 840 tained designs, a post-evaluation in a commercial soft-
 841 ware using a segregated approach would indeed be rel-
 842 evant. However, we have so far not been successful in
 843 developing a methodology able to transfer the complex
 844 optimized designs for further processing. Thus, the ob-
 845 tained designs may at present remain inspirational for
 846 future heat exchanger designs.

847 In this first work on systematic heat-exchanger de-
 848 sign with well-defined wall-thickness using topology
 849 optimization, we have focused on method development
 850 and providing examples with ultimate design freedom,

851 which amongst others resulted in the interesting appear-
 852 ance of microvillies. Such intricate geometrical details
 853 will probably not be relevant for practical systems, but
 854 give valuable insight. As discussed above, such de-
 855 tails may also be difficult to handle geometrically - also
 856 manufacturing-wise, even with advance additive man-
 857 ufacturing techniques. To hinder such complexity and
 858 ensure manufacturability, we may in future work in-
 859 clude more restrictive geometry constraints like larger
 860 length-scale, overhang or extrusion constraints, keeping
 861 in mind that every constraint imposed will decrease the
 862 achievable heat exchanger efficiencies.

863 Acknowledgements

864 The authors gratefully acknowledge the financial sup-
 865 port of the Villum Foundation through the Villum Inves-
 866 tigator project InnoTop.

Appendix A. Weak formulations and stabilization parameters

Appendix A.1. Mass transfer

The weak form of the Navier-Stokes equations (1,2) is to be found in the following. For this purpose, the finite dimensional trial- and test function spaces for the velocity, \mathcal{S}_u and \mathcal{V}_u , and for the pressure, \mathcal{S}_p and \mathcal{V}_p , respectively, are introduced. The trial functions $u_i \in \mathcal{S}_u$ and $p \in \mathcal{S}_p$ shall be found such that the test functions $\forall w_i \in \mathcal{V}_u$ and $\forall q \in \mathcal{V}_p$. After multiplication by the test functions, the expressions are integrated over the volume Ω .

After integration by parts with the assumption of no outward surface traction, the weak form yields:

$$\begin{aligned}
\mathcal{R}^u &= \int_{\Omega} w_i u_i \frac{\partial u_j}{\partial x_i} dV + \int_{\Omega} \frac{1}{Re} \frac{\partial w_i}{\partial x_j} \left(\frac{\partial u_i}{\partial x_j} + \frac{\partial u_j}{\partial x_i} \right) dV \\
&\quad - \int_{\Omega} \frac{\partial w_i}{\partial x_i} P dV + \int_{\Omega} w_i \alpha u_i dV = 0 \\
\mathcal{R}^p &= \int_{\Omega} q \frac{\partial u_i}{\partial x_i} dV = 0
\end{aligned} \tag{A.1}$$

As discussed in Section 4, the residual functionals are stabilised, by adding both SUPG and PSPG stabilisations, \mathcal{F}^δ and \mathcal{F}^ϵ , respectively:

$$\begin{aligned}
\tilde{\mathcal{R}}^u &= \mathcal{R}^u + \mathcal{F}^\delta = 0 \\
\tilde{\mathcal{R}}^p &= \mathcal{R}^p + \mathcal{F}^\epsilon = 0
\end{aligned} \tag{A.2}$$

The weak SUPG- and PSPG stabilisation terms are given as a function of R_i^u , the residual from the strong form Navier-Stokes formulation [51]:

$$\mathcal{F}^\delta = \sum_{e=1}^{N_e} \int_{\Omega_e} \tau_{SU} u_i \frac{\partial w_j}{\partial x_i} R_j^u dV \tag{A.3}$$

$$\mathcal{F}^\epsilon = \sum_{e=1}^{N_e} \int_{\Omega_e} \tau_{PS} \frac{\partial q}{\partial x_j} R_j^u dV \tag{A.4}$$

The stabilization factors, τ_{SU} and τ_{PS} , used for the mass transfer problems SUPG and PSPG stabilization, respectively, are the same. It is almost identical to the one used by [24]:

$$\tau_{SU} = \tau_{PS} = \tau = \left(\frac{1}{\tau_1^r} + \frac{1}{\tau_3^r} + \alpha^r \right)^{-\frac{1}{r}} \tag{A.5}$$

where the power in the minimum function is set to $r = 2$. The factors are given as:

$$\tau_1 = \frac{4h_e}{\|\mathbf{u}_e\|_2} \tag{A.6}$$

$$\tau_3 = \frac{h_e^2 Re}{4} \tag{A.7}$$

The derivatives of the stabilization parameter with respect the velocity state and to the design variable, used for the computation of the Jacobian matrix and of the sensitivities, are given as:

$$\frac{\partial \tau}{\partial \mathbf{u}_e} = \frac{1}{\tau_1^3} \left(\frac{1}{\tau_1^2} + \frac{1}{\tau_3^2} + \alpha^2 \right)^{-\frac{3}{2}} \left(-\tau_1 (\mathbf{u}_e^T \mathbf{u}_e)^{-1} \mathbf{u}_e^T \right) \tag{A.8}$$

$$\frac{\partial \tau}{\partial \xi} = -\alpha \left(\frac{1}{\tau_1^2} + \frac{1}{\tau_3^2} + \alpha^2 \right)^{-\frac{3}{2}} \frac{\partial \alpha}{\partial \xi} \tag{A.9}$$

Appendix A.2. Heat transfer

The weak form of the heat transfer problem from (6) is obtained by introducing the trial- and test function spaces, \mathcal{S}_T and \mathcal{V}_T , respectively. The finite element problem hence translates to finding a temperature field (trial function) $T \in \mathcal{S}_T$, such that the test function $\forall v \in \mathcal{V}_T$. After integration by part, and assuming no outward surface heat flux (i.e. the domain is insulated), the variational formulation yields.

$$\mathcal{R}^T = \int_{\Omega} v \sum_{\gamma=1}^{NF} (Pe_s^\gamma u_i^\gamma) \frac{\partial T}{\partial x_i} dV + \int_{\Omega} C_k \frac{\partial v}{\partial x_i} \frac{\partial T}{\partial x_i} dV = 0 \tag{A.10}$$

The residual is stabilised with a SUPG stabilisation scheme, \mathcal{F}^ζ :

$$\tilde{\mathcal{R}}^T = \mathcal{R}^T + \mathcal{F}^\zeta = 0 \tag{A.11}$$

As in the mass transfer, the weak stabilization term is given as a function of the strong for residual R_i^T , obtained from (6), as well as the convection term, $\sum_{\gamma=1}^{NF} (Pe_s^\gamma u_i^\gamma)$:

$$\mathcal{F}^\zeta = \sum_e^{N_e} \int_{\Omega_e} \tau_{SU_T} \sum_{\gamma=1}^{NF} (Pe_s^\gamma u_i^\gamma) \frac{\partial v}{\partial x_i} R_i^T dV \tag{A.12}$$

The factor for the SUPG stabilization of the heat transfer, τ_{SU_T} , is given as used by [24]:

$$\tau_{SU_T} = \left(\frac{1}{\tau_{1,T}^r} + \frac{1}{\tau_{3,T}^r} \right)^{-\frac{1}{r}} \tag{A.13}$$

where the power in the min function is set to $r = 2$. The factors are given as:

$$\tau_{1,T} = \frac{4h_e}{\left\| \left(\mathbf{u}_e^1 Pe^1 + \mathbf{u}_e^2 Pe^2 \right) \right\|_2} \tag{A.14}$$

$$\tau_{3,T} = \frac{h_e^2}{4C_k} \tag{A.15}$$

The velocity and design variable derivatives of the stabilization parameters are:

$$\frac{\partial \tau_{SU_T}}{\partial \mathbf{u}_e^\gamma} = -\tau_{SU_T}^3 \frac{Pe^\gamma}{16h_e^2} \left(\mathbf{u}_e^1 Pe^1 + \mathbf{u}_e^2 Pe^2 \right) \tag{A.16}$$

$$\frac{\partial \tau_{SU_T}}{\partial \xi} = \frac{1}{\tau_{3,T}^3} \left(\frac{1}{\tau_{1,T}^2} + \frac{1}{\tau_{3,T}^2} \right)^{-\frac{3}{2}} \left(-\frac{h_e^2}{4C_k} \right) \frac{\partial C_k}{\partial \xi} \tag{A.17}$$

Appendix B. Notes on sensitivity analysis

Appendix B.1. Adjoint sensitivity analysis

In order to find the sensitivities of a function, the Lagrangian function, with the arbitrary Lagrangian multipliers, as seen in Equation (24), is set up. Differentiating this function with respect to the design variable, and invoking the chain rule on all terms gives:

$$\begin{aligned} \frac{d\mathcal{L}}{d\xi} = \frac{\partial\Phi}{\partial\xi} + \sum_{s=\{F1, F2, T\}} \left(\frac{\partial\Phi}{\partial\mathbf{s}} \frac{d\mathbf{s}}{d\xi} + \right. \\ \left. \lambda_s^\top \frac{\partial\mathbf{R}_s}{\partial\xi} + \lambda_s^\top \frac{\partial\mathbf{R}_s}{\partial\mathbf{u}_1} \frac{d\mathbf{u}_1}{d\xi} + \right. \\ \left. \lambda_s^\top \frac{\partial\mathbf{R}_s}{\partial\mathbf{u}_2} \frac{d\mathbf{u}_2}{d\xi} + \lambda_s^\top \frac{\partial\mathbf{R}_s}{\partial T} \frac{dT}{d\xi} \right) \end{aligned} \quad (\text{B.1})$$

where the summation over s signifies, that the operation is repeated for both mass transfer- and the heat transfer state. As the two mass transfer states are mutually independent, and the coupling between the two mass transfers is weak, the corresponding terms in (B.1) can be left out. The Lagrangian multipliers, being arbitrary allows to set certain terms to zero:

$$\begin{aligned} \frac{d\mathcal{L}}{d\xi} = \frac{\partial\Phi}{\partial\xi} + \lambda_{F1}^\top \frac{\partial\mathbf{R}_{F1}}{\partial\xi} + \lambda_{F2}^\top \frac{\partial\mathbf{R}_{F2}}{\partial\xi} + \lambda_T^\top \frac{\partial\mathbf{R}_T}{\partial\xi} \\ + \underbrace{\left(\frac{\partial\Phi}{\partial\mathbf{u}_1} + \lambda_{F1}^\top \frac{\partial\mathbf{R}_{F1}}{\partial\mathbf{u}_1} + \lambda_T^\top \frac{\partial\mathbf{R}_T}{\partial\mathbf{u}_1} \right)}_{=0} \frac{d\mathbf{u}_1}{d\xi} \\ + \underbrace{\left(\frac{\partial\Phi}{\partial\mathbf{u}_2} + \lambda_{F2}^\top \frac{\partial\mathbf{R}_{F2}}{\partial\mathbf{u}_2} + \lambda_T^\top \frac{\partial\mathbf{R}_T}{\partial\mathbf{u}_2} \right)}_{=0} \frac{d\mathbf{u}_2}{d\xi} \\ + \underbrace{\left(\frac{\partial\Phi}{\partial T} + \lambda_T^\top \frac{\partial\mathbf{R}_T}{\partial T} \right)}_{=0} \frac{dT}{d\xi} \end{aligned} \quad (\text{B.2})$$

which hence allows for the elimination of the difficult terms $\frac{d\mathbf{u}_1}{d\xi}$, $\frac{d\mathbf{u}_2}{d\xi}$ and $\frac{dT}{d\xi}$, by solving the adjoint problems, outlined in Equations (26-28). The sensitivities are then found using the Lagrangian multipliers computed by solving the adjoint problems, as seen in Equation (25).

Appendix B.2. Chain rule projection of sensitivities

The sensitivities of the objective function, and of the constraints, are found with respect to ξ_1 and ξ_2 , as described in Section 5.5 and Appendix B.1. These sensitivities $\frac{\partial\Phi}{\partial\xi_1}$ and $\frac{\partial\Phi}{\partial\xi_2}$, are projected back to $\frac{\partial\Phi}{\partial\xi}$ using the chain rule:

$$\frac{\partial\Phi}{\partial\xi} = \frac{\partial\Phi}{\partial\xi} + \frac{d\Phi}{d\xi_1} \frac{\partial\xi_1}{\partial\xi} + \frac{d\Phi}{d\xi_2} \frac{\partial\xi_2}{\partial\xi} \quad (\text{B.3})$$

The sensitivities with respect to the eroded and dilated variables are projected back to the design variable ξ with steps corresponding to the one of the erosion dilation process from Section 5.3. Keeping in mind that $\frac{\partial\xi_1}{\partial\xi} = -1$, the chain-rule terms are given as:

$$\frac{\partial\xi_1}{\partial\xi} = -\frac{\partial\hat{\xi}_1}{\partial\hat{\xi}} \frac{\partial\hat{\xi}}{\partial\tilde{\xi}} \frac{\partial\tilde{\xi}}{\partial\xi} \quad (\text{B.4})$$

$$\frac{\partial\xi_2}{\partial\xi} = \frac{\partial\hat{\xi}_2}{\partial\hat{\xi}} \frac{\partial\hat{\xi}}{\partial\tilde{\xi}} \frac{\partial\tilde{\xi}}{\partial\xi} \quad (\text{B.5})$$

The chain rule terms $\frac{\partial\hat{\xi}_y}{\partial\hat{\xi}}$ and $\frac{\partial\tilde{\xi}}{\partial\hat{\xi}}$ are found by differentiation of the smooth Heaviside projection from Equation (18):

$$\frac{\partial\tilde{\xi}}{\partial\hat{\xi}} = \beta \frac{1 - \tanh^2(\beta(\tilde{\xi} - \eta))}{\tanh(\beta\eta) + \tanh(\beta(1 - \eta))} \quad (\text{B.6})$$

The filtering operation terms from the chain rule, $\frac{\partial\tilde{\xi}}{\partial\hat{\xi}}$ and $\frac{\partial\hat{\xi}}{\partial\xi}$, are equivalent to filtering the sensitivities through the PDE filter, as was done with ξ to obtain $\tilde{\xi}$ and with $\tilde{\xi}$ to obtain $\hat{\xi}$ [42].

Appendix C. Counter-flow heat exchanger on a finer mesh

In order to verify that the discretization of the 2 dimensional counter-flow heat exchanger domain is adequate, the example, discussed in Section 6.1, is re-run on a refined mesh of $648 \times 144 \times 1$ cubic elements. The cases with $\Delta P_{max} = 5 \Delta P_{base}$, with both initial designs, are considered in this experiment. The obtained designs, seen in Figure 21, have similar features as the corresponding ones in Figures 7c and 7d.

The objective functions from the structures obtained using the finer mesh, seen in Figure 21, deviate by 0.08%-2.23% from the ones obtained under corresponding conditions on the coarser discretization seen in Figures 7c-d. The topologies appear to be similar and it is difficult to attribute the differences to either the design or the mesh refinements.

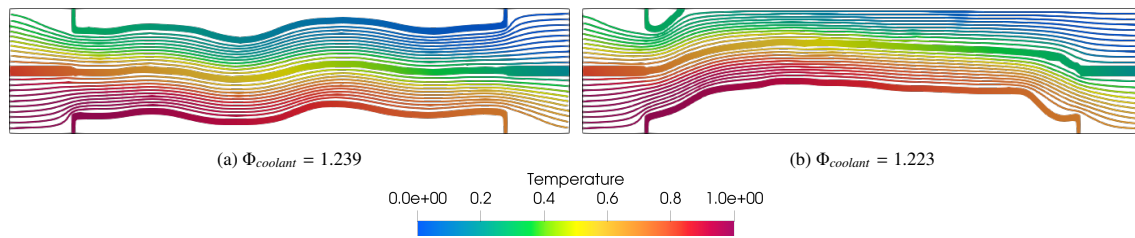


Figure 21: Designs obtained with $\Delta P_{max} = 5 \Delta P_{base}$, when using a refined mesh with $(648 \times 144 \times 1)$ cubic elements. The optimization was carried using the two different initial designs, (a) parallel channels and (b) $\xi = 0.5$. Structures are thresholded at $\alpha^1 > 0.1\bar{\alpha}^1 \wedge \alpha^2 > 0.1\bar{\alpha}^2$.

References

- [1] F. P. Incropera, Foundations of heat transfer, 6., international student version ed., John Wiley, Singapore, 2013.
- [2] M. Awais, A. A. Bhuiyan, Heat and mass transfer for compact heat exchanger (chxs) design: A state-of-the-art review, International Journal of Heat and Mass Transfer 127 (2018) 359 – 380. doi:<https://doi.org/10.1016/j.ijheatmasstransfer.2018.08.026>.
- [3] M. M. A. Bhutta, N. Hayat, M. H. Bashir, A. R. Khan, K. N. Ahmad, S. Khan, Cfd applications in various heat exchangers design: A review, Applied Thermal Engineering 32 (2012) 1 – 12. doi:<https://doi.org/10.1016/j.applthermaleng.2011.09.001>.
- [4] Conflux, Conflux technology website, <https://www.confluxtechnology.com/>, 2020. Accessed: 02-05-2020.
- [5] nTopology, Taking Heat Exchanger Design to the Next Level with High-Performance Geometry - nTopology blog entry, <https://ntopology.com/blog/2019/12/16/taking-heat-exchanger-design-to-the-next-level-with-high-performance-geometry/>, 2019. Accessed: 02-05-2020.
- [6] Y. Luo, Q. Li, S. Liu, Topology optimization of shell-infill structures using an erosion-based interface identification method, Computer Methods in Applied Mechanics and Engineering 355 (2019) 94–112. doi:[10.1016/j.cma.2019.05.017](https://doi.org/10.1016/j.cma.2019.05.017).
- [7] M. P. Bendsøe, N. Kikuchi, Generating optimal topologies in structural design using a homogenization method, Computer Methods in Applied Mechanics and Engineering 71 (1988) 197–224. doi:[10.1016/0045-7825\(88\)90086-2](https://doi.org/10.1016/0045-7825(88)90086-2).
- [8] O. Sigmund, K. Maute, Topology optimization approaches: A comparative review, Structural and Multidisciplinary Optimization 48 (2013) 1031–1055. doi:[10.1007/s00158-013-0978-6](https://doi.org/10.1007/s00158-013-0978-6).
- [9] J. Alexandersen, C. S. Andreasen, A review of topology optimisation for fluid-based problems, Fluids 5 (2020) 1–32. doi:[10.3390/fluids5010029](https://doi.org/10.3390/fluids5010029).
- [10] T. Borrvall, J. Petersson, Topology optimization of fluids in stokes flow, International Journal for Numerical Methods in Fluids 41 (2003) 77–107. doi:[10.1002/flid.426](https://doi.org/10.1002/flid.426).
- [11] N. Aage, T. H. Poulsen, A. Gersborg-Hansen, O. Sigmund, Topology optimization of large scale stokes flow problems, Structural and Multidisciplinary Optimization 35 (2008) 175–180. doi:[10.1007/s00158-007-0128-0](https://doi.org/10.1007/s00158-007-0128-0).
- [12] V. J. Challis, J. K. Guest, Level set topology optimization of fluids in stokes flow, International Journal for Numerical Methods in Engineering 79 (2009) 1284–1308. doi:[10.1002/nme.2616](https://doi.org/10.1002/nme.2616).
- [13] A. Evgrafov, State space newton’s method for topology optimization, Computer Methods in Applied Mechanics and Engineering 278 (2014) 272–290. doi:[10.1016/j.cma.2014.06.005](https://doi.org/10.1016/j.cma.2014.06.005).
- [14] K. Yonekura, Y. Kanno, Topology optimization method for interior flow based on transient information of the lattice boltzmann method with a level-set function, Japan Journal of Industrial and Applied Mathematics 34 (2017) 611–632. doi:[10.1007/s13160-017-0257-9](https://doi.org/10.1007/s13160-017-0257-9).
- [15] C. H. Villanueva, K. Maute, Cutfem topology optimization of 3d laminar incompressible flow problems, Computer Methods in Applied Mechanics and Engineering 320 (2017) 444–473. doi:[10.1016/j.cma.2017.03.007](https://doi.org/10.1016/j.cma.2017.03.007).
- [16] C. Chen, K. Yaji, T. Yamada, K. Izui, S. Nishiwaki, Local-in-time adjoint-based topology optimization of unsteady fluid flows using the lattice boltzmann method, Mechanical Engineering Journal 4 (2017) 17–00120–17–00120. doi:[10.1299/mej.17-00120](https://doi.org/10.1299/mej.17-00120).
- [17] C. B. Dilgen, S. B. Dilgen, D. R. Fuhrman, O. Sigmund, B. S. Lazarov, Topology optimization of turbulent flows, Computer Methods in Applied Mechanics and Engineering 331 (2018) 363–393. doi:[10.1016/j.cma.2017.11.029](https://doi.org/10.1016/j.cma.2017.11.029).
- [18] L. Łaniewski Wołk, J. Rokicki, Adjoint lattice boltzmann for topology optimization on multi-gpu architecture, Computers & Mathematics with Applications 71 (2016) 833–848. doi:[10.1016/j.camwa.2015.12.043](https://doi.org/10.1016/j.camwa.2015.12.043).
- [19] J. H. Haertel, G. F. Nellis, A fully developed flow thermo-fluid model for topology optimization of 3d-printed air-cooled heat exchangers, Applied Thermal Engineering 119 (2017) 10–24. doi:[10.1016/j.applthermaleng.2017.03.030](https://doi.org/10.1016/j.applthermaleng.2017.03.030).
- [20] J. H. Haertel, K. Engelbrecht, B. S. Lazarov, O. Sigmund, Topology optimization of a pseudo 3d thermo-fluid heat sink model, International Journal of Heat and Mass Transfer 121 (2018) 1073–1088. doi:[10.1016/j.ijheatmasstransfer.2018.01.078](https://doi.org/10.1016/j.ijheatmasstransfer.2018.01.078).
- [21] K. Yaji, M. Ogino, C. Chen, K. Fujita, Large-scale topology optimization incorporating local-in-time adjoint-based method for unsteady thermal-fluid problem, Structural and Multidisciplinary Optimization 58 (2018) 817–822. doi:[10.1007/s00158-018-1922-6](https://doi.org/10.1007/s00158-018-1922-6).
- [22] S. B. Dilgen, C. B. Dilgen, D. R. Fuhrman, O. Sigmund, B. S. Lazarov, Density based topology optimization of turbulent flow heat transfer systems, Structural and Multidisciplinary Optimization 57 (2018) 1905–1918. doi:[10.1007/s00158-018-1967-6](https://doi.org/10.1007/s00158-018-1967-6).
- [23] M. Pietropaoli, F. Montomoli, A. Gaymann, Three-dimensional fluid topology optimization for heat transfer, Structural and Multidisciplinary Optimization 59 (2019) 801–812. doi:[10.1007/s00158-018-2102-4](https://doi.org/10.1007/s00158-018-2102-4).
- [24] J. Alexandersen, O. Sigmund, N. Aage, Large scale three-dimensional topology optimisation of heat sinks cooled by natural convection, International Journal of Heat and Mass Transfer 100 (2016) 876–891. doi:[10.1016/j.ijheatmasstransfer.2016.05.013](https://doi.org/10.1016/j.ijheatmasstransfer.2016.05.013).
- [25] J. Alexandersen, O. Sigmund, K. E. Meyer, B. S. Lazarov,

- Design of passive coolers for light-emitting diode lamps using topology optimisation, *International Journal of Heat and Mass Transfer* 122 (2018) 138–149. doi:10.1016/j.ijheatmasstransfer.2018.01.103.
- [26] N. Pollini, O. Sigmund, C. S. Andreasen, J. Alexandersen, A “poor man’s” approach for high-resolution three-dimensional topology design for natural convection problems, *Advances in Engineering Software* 140 (2020) 102736. doi:https://doi.org/10.1016/j.advengsoft.2019.102736.
- [27] C. Sun, N. Lewpiriyawong, K. L. Khoo, S. Zeng, P. S. Lee, Thermal enhancement of fin and tube heat exchanger with guiding channels and topology optimisation, *International Journal of Heat and Mass Transfer* 127 (2018) 1001–1013. doi:10.1016/j.ijheatmasstransfer.2018.08.093.
- [28] H. Kobayashi, K. Yaji, S. Yamasaki, K. Fujita, Freeform winglet design of fin-and-tube heat exchangers guided by topology optimization, *Applied Thermal Engineering* 161 (2019). doi:10.1016/j.applthermaleng.2019.114020.
- [29] P. Papazoglou, *Topology Optimization of Heat Exchangers*, Master’s thesis, Delft University of Technology, 2015. URL: <http://resolver.tudelft.nl/uuid:08481ec6-d6df-4162-b254-8b99ecccc6d1>.
- [30] J. Haertel, *Design of Thermal Systems Using Topology Optimization*, Ph.D. thesis, Technical University of Denmark, 2018. URL: <https://orbit.dtu.dk/en/publications/design-of-thermal-systems-using-topology-optimization>.
- [31] R. Tawk, B. Ghannam, M. Nemer, Topology optimization of heat and mass transfer problems in two fluids—one solid domains, *Numerical Heat Transfer, Part B: Fundamentals* 76 (2019) 1–22. doi:10.1080/10407790.2019.1644919.
- [32] K. R. Saviers, R. Ranjan, R. Mahmoudi, Design and validation of topology optimized heat exchangers, in: *AIAA Scitech 2019 Forum*, American Institute of Aeronautics and Astronautics, Reston, Virginia, 2019, p. 7 pp. doi:10.2514/6.2019-1465.
- [33] H. Kobayashi, K. Yaji, S. Yamasaki, K. Fujita, Topology design of two-fluid heat exchange (2020). URL: <https://arxiv.org/abs/2005.08870>. arXiv:2005.08870.
- [34] A. Clausen, N. Aage, O. Sigmund, Topology optimization of coated structures and material interface problems, *Computer Methods in Applied Mechanics and Engineering* 290 (2015) 524–541. doi:10.1016/j.cma.2015.02.011.
- [35] A. Clausen, E. Andreassen, O. Sigmund, Topology optimization of 3d shell structures with porous infill, *Acta Mechanica Sinica* 33 (2017) 778–791. doi:10.1007/s10409-017-0679-2.
- [36] A. Gersborg-Hansen, O. Sigmund, R. Haber, Topology optimization of channel flow problems, *Structural and Multidisciplinary Optimization* 30 (2005) 181–192. doi:10.1007/s00158-004-0508-7.
- [37] A. Evgrafov, The limits of porous materials in the topology optimization of stokes flows, *Applied Mathematics and Optimization* 52 (2005) 263–277. doi:10.1007/s00245-005-0828-z.
- [38] L. H. Olesen, F. Okkels, H. Bruus, A high-level programming-language implementation of topology optimization applied to steady-state navier-stokes flow, *International Journal for Numerical Methods in Engineering* 65 (2006) 975–1001. doi:10.1002/nme.1468.
- [39] K. Svanberg, The method of moving asymptotes - a new method for structural optimization, *International Journal for Numerical Methods in Engineering* 24 (1987).
- [40] N. Aage, E. Andreassen, B. S. Lazarov, Topology optimization using petsc: An easy-to-use, fully parallel, open source topology optimization framework, *Structural and Multidisciplinary Optimization* 51 (2015) 565–572. doi:10.1007/s00158-014-1157-0.
- [41] O. Sigmund, J. Petersson, Numerical instabilities in topology optimization: A survey on procedures dealing with checkerboards, mesh-dependencies and local minima, *Structural Optimization* 16 (1998) 68–75. doi:10.1007/BF01214002.
- [42] B. S. Lazarov, O. Sigmund, Filters in topology optimization based on helmholtz-type differential equations, *International Journal for Numerical Methods in Engineering* 86 (2011) 765–781. doi:10.1002/nme.3072.
- [43] F. Wang, B. S. Lazarov, O. Sigmund, On projection methods, convergence and robust formulations in topology optimization, *Structural and Multidisciplinary Optimization* 43 (2011) 767–784. doi:10.1007/s00158-010-0602-y.
- [44] M. Stolpe, K. Svanberg, An alternative interpolation scheme for minimum compliance topology optimization, *Structural and Multidisciplinary Optimization* 22 (2001) 116–124. doi:10.1007/s001580100129.
- [45] J. Alexandersen, *Topology Optimisation for Coupled Convection Problems*, Ph.D. thesis, Technical University of Denmark, 2013.
- [46] M. P. Bendsøe, O. Sigmund, Material interpolation schemes in topology optimization, *Archive of Applied Mechanics* 69 (1999) 635–654. doi:10.1007/s004190050248.
- [47] J. K. Guest, A. Asadpoure, S.-H. Ha, Eliminating beta-continuation from Heaviside projection and density filter algorithms, *Structural and Multidisciplinary Optimization* 44 (2011) 443–453. doi:10.1007/s00158-011-0676-1.
- [48] J. Alexandersen, B. S. Lazarov, Topology optimisation of manufacturable microstructural details without length scale separation using a spectral coarse basis preconditioner, *Computer Methods in Applied Mechanics and Engineering* 290 (2015) 156–182. doi:10.1016/j.cma.2015.02.028.
- [49] K. Thulukkanam, *Heat Exchanger Design Handbook*, CRC Press, 2013. doi:10.1201/b14877.
- [50] E. Ozden, I. Tari, Shell side CFD analysis of a small shell-and-tube heat exchanger, *Energy Conversion and Management* 51 (2010) 1004–1014. doi:https://doi.org/10.1016/j.enconman.2009.12.003.
- [51] J. Alexandersen, N. Aage, C. S. Andreasen, O. Sigmund, Topology optimisation for natural convection problems, *International Journal for Numerical Methods in Fluids* 76 (2014) 699–721. doi:10.1002/flid.3954.